

Effect of the vertical inflow conditions on the evolution of liquid films on rotating disks

Diploma thesis

Author: Richard Markl

Submitted to
Graz University of Technology
Faculty for Mechanical Engineering

for receiving the academic degree

Diplomingenieur

Supervisor: Ao.Univ.-Prof. Dipl.-Ing. Dr.techn. Helfried Steiner
Institute of Fluid Mechanics and Heat Transfer
Graz University of Technology

Graz, January 2013

Deutsche Fassung:

Beschluss der Curricula-Kommission für Bachelor-, Master- und Diplomstudien
vom 10.11.2008

Genehmigung des Senates am 1.12.2008

EIDESSTATTLICHE ERKLÄRUNG

Ich erkläre an Eides statt, dass ich die vorliegende Arbeit selbstständig verfasst, andere als die angegebenen Quellen/Hilfsmittel nicht benutzt, und die den benutzten Quellen wörtlich und inhaltlich entnommene Stellen als solche kenntlich gemacht habe.

Graz, am.....

(Ort, Datum)

.....

(Unterschrift)

Englische Fassung:

STATUTORY DECLARATION

I declare that I have authored this thesis independently, that I have not used other than the declared sources / resources, and that I have explicitly marked all material which has been quoted either literally or by content from the used sources.

Graz, at.....

(location, date)

.....

(signature)

Vorwort und Danksagung

Einleitend zu dieser Arbeit möchte ich mich gerne bei all jenen bedanken, die mir dabei geholfen haben, diese Arbeit fertigzustellen, besonders bei meinem Betreuer ao. Univ.-Prof. Dr. Helfried Steiner, für seine tatkräftige Unterstützung, der Firma Lam Research, die mir diese Arbeit ermöglicht hat und den Mitarbeitern des Instituts für Strömungslehre und Wärmeübertragung, die mir bei etwaigen Fragen gerne zu Verfügung gestanden sind.

Ein großes Dankeschön geht auch an meine Freunde und Wegbegleiter während des Studiums. Hervorheben möchte ich hier speziell meine Freundin Julia, die mich immer wieder motiviert hat und meine Schwester Katharina.

Meine Eltern sind mir jederzeit im Studium zur Seite gestanden und waren auch immer wichtige Ratgeber fürs Leben. Ihnen ist diese Arbeit gewidmet.

Kurzfassung

Die vorliegende Arbeit beschäftigt sich mit der numerischen Simulation der Strömung von flüssigen Filmen auf rotierenden Scheiben. Die untersuchte Problemstellung ist von großer praktischer Relevanz in der sogenannten Nassprozessstechnik, beispielsweise zur Oberflächenbehandlung (Ätzen, Spülen, Reinigen) von Silizium-Wafern in der Halbleiterindustrie. Der Fokus der rechnerischen Untersuchungen lag auf der Analyse der Strömungsverhältnisse in der Nähe der Drehachse der Scheibe, wo die Prozessflüssigkeit durch einen vertikalen Freistrahler aufgetragen wird. Wesentliches Ziel der Simulationen war die Darstellung des Einflusses des Abstands der vertikalen Auftragsdüse von der Scheibe auf die resultierende Filmströmung unter Variation der Drehzahl und des aufgetragenen Volumenstroms. Basierend auf den Simulationsergebnissen konnte der Radius einer zentralen Einflusszone definiert und parametrisiert werden, wo die vorgegebenen vertikalen Zuströmbedingungen (Düsenhöhe, turbulenter/laminarer Strömungszustand) relevant sind und deren konkrete Auswirkungen auf die Strömung durch die Simulationen detailliert beschrieben werden. Außerhalb der zentralen Einflusszone erwies sich die Filmströmung als praktisch unabhängig von den Zuströmbedingungen, im wesentlichen als laminar, und lediglich abhängig von der Drehzahl und dem Volumenstrom. Der Vergleich der Simulationsergebnisse mit ebenso berechneten Näherungslösungen, welche auf der Dünnschichtnäherung über die Filmdicke gemittelter Formulierung basieren, zeigte gute Übereinstimmung im äußeren Bereich der Scheibe. Für die im Bereich der zentralen Einflusszone beobachteten Abweichungen konnten die in den Näherungslösungen anzunehmenden Geschwindigkeitsprofile als wesentliche Ursache identifiziert werden. Die hierbei typischerweise angenommenen Polynome konnten insbesondere die turbulenten Profile nur unzulänglich annähern. Eine mögliche Verbesserung der grundsätzlich guten Vorhersagekapazität der Näherungslösungen legt daher eine geeignete Anpassung der Profilannahmen im turbulenten Strömungsregime nahe.

Abstract

The present thesis investigates the flow of liquid films on rotating disks using numerical simulations. The examined problem is of high practical relevance in the so called wet-processing technology, as it is applied, e.g., in the surface processing (etching, cleansing, cleaning) of silicon-wafers in the semiconductor industry. The focus of the computational investigation is on the analysis of the flow conditions near the axis of rotation of the disk, where the processing liquid is supplied by a vertical free jet. The simulations essentially aim to examine the influence of the distance between the jet exit nozzle and the disk on the resulting film flow at varying rotational speeds and volumetric flow rates of the dispensed liquid. Based on the results of the simulations the radius of a central region of influence could be defined and parameterized, where the given vertical inflow conditions (nozzle-to-disk distance, turbulent/laminar flow conditions) are relevant, as their effect on the flow is clearly indicated by the simulations. Outside of the central region of influence, the film flow is shown to be practically independent of the inflow conditions, mostly laminar, and only dependent of the rotational speed and the volumetric flow rate. The comparison of the results of the simulations with approximate solutions which were computed based on the thin-film approximation using a depth-averaged formulation showed good agreement in the outer radial region of the disk. The disagreement observed in the impingement region near the center could be mainly attributed to the assumptions for the velocity profiles, which are required by the depth-averaged approximation methods. The assumed polynomials particularly missed the bulky profiles typically occurring in the turbulent flow regime. An appropriate adaptation of the profile assumptions in the turbulent flow regime appears therefore as a consequent step to further improve the predictive capability of the depth-averaged solution obtained in the thin film approximation.

Contents

1	Introduction	1
1.1	Background and motivation	1
1.2	Objectives	3
2	Numerical Simulation	6
2.1	Basic equations of fluid mechanics	6
2.2	Multiphase model	7
2.3	Turbulence Models	12
2.3.1	Realizable k - ϵ	15
2.3.2	SST k - ω	20
2.4	Numerical solution	24
2.4.1	Discretization in space	24
2.4.2	Solver settings	27
2.4.3	Computational domain and discretization	28
2.4.4	Boundary conditions	31
3	Approximate Solutions	33
3.1	Thin Film Equations	33
3.2	Pigford model	40
4	Results	42
4.1	Considered test cases	42
4.2	Numerical results	43
4.2.1	Centerline velocity of the impinging liquid jet	43
4.2.2	Film thickness and mean radial velocity	47
4.2.3	Wall shear stress	51
4.2.4	Local velocity profiles inside the liquid film	54
4.2.5	Effect of turbulence	55
4.3	Comparison against approximate solutions	63
5	Summary	72
	List of symbols	74

References

78

1 Introduction

1.1 Background and motivation

The company Lam Research located at Villach develops and manufactures machines used in the semiconductor industry for the processing of silicon wafers. Several single-sided surface processing steps such as cleaning and etching are performed on these devices. The whole process is essentially based on the spreading of the operating liquid over the rotating disk in form of a thin liquid film driven by centrifugal forces. The operating liquid is supplied by a vertical jet, which vertically impinges on the surface. The typically realized flow configuration is sketched in Figure 1.

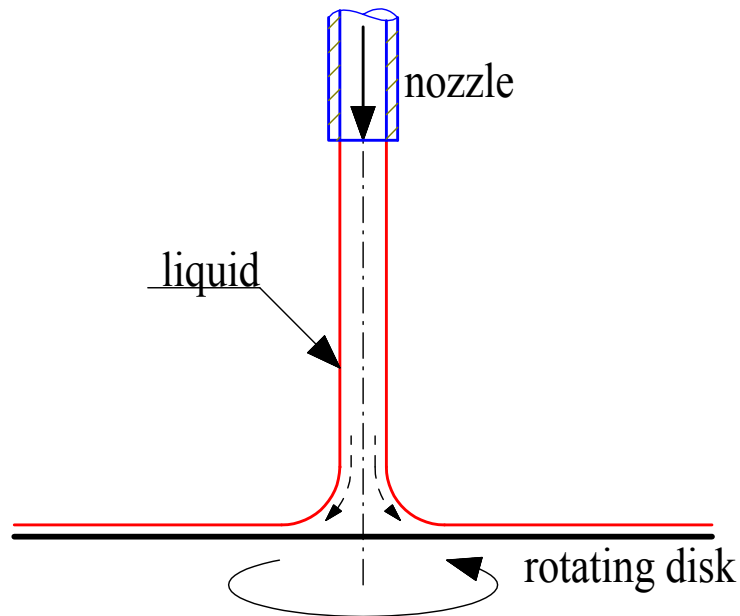


Figure 1: Sketch of the impinging jet on the rotating disk

A most comprehensive knowledge of the flow conditions along the surface is important for the outcome of the process. This is specially true for the region of impingement, where the oncoming vertical momentum of the liquid jet is abruptly redirected into the horizontal direction. The present work puts the focus on the fairly complex flow emerging from the point of impingement,

which is hardly accessible to experimental measurements. In particular, it numerically investigates the influence the vertical inflow conditions in terms of laminar/turbulent inflow and the nozzle-to-disk height. While the first is basically predetermined by the volumetric flow rate of the liquid fluid, the latter has been to date merely determined on empirical or practical grounds. Photos recorded with a high-speed camera displayed in Figures 2 and 3 exemplary show a laminar and a turbulent case, where the nozzle, the jet and the disk covered by a wavy liquid film are clearly visible. In the case with turbulent inflow conditions shown in Figure 3 the film surface evidently exhibits a more irregular wave pattern.



Figure 2: Laminar impinging jet on the rotating disk, $n = 200 \text{ rpm}$, $Q = 0.3 \text{ lpm}$



Figure 3: Turbulent impinging jet on the rotating disk, $n = 200 \text{ rpm}$, $Q = 1.2 \text{ lpm}$

Although there exist quite a lot of literature on the computational investigation of liquid film flow on rotating disks (see, e.g., Sisoiev *et al.* (2003), Kim & Kim (2009), Liu *et al.* (1991)), the region of liquid impingement is mostly excluded. This is partly due the fact the many author analyzed the flow based on the so called thin film approximation, which is not applicable to the region of impingement. This restriction does basically not apply to the work of Rice *et al.* (2005), who performed a VOF-based axisymmet-

ric simulation of the flow including heat transfer. However, they considered in their simulations a very special configuration, which was experimentally investigated by Ozar *et al.* (2003), where the liquid is horizontally supplied through an annular nozzle. In this particular case the radial inner boundary is represented by the radial exit of the nozzle with the nozzle height being the initial film height, and there is clearly no impingement region. Nonetheless, some experimental and computational works can still be found, which consider the impingement region as well. Among these are the studies of Miyasaka (1974*a,b*) who investigated the radially inner flow region computationally as well as experimentally. Landreth & Adrian (1990) used particle image velocimetry (PIV) to measure many instantaneous velocity fields near the impingement region of a submerged water jet vertically directed to a horizontal plate at rest. Considering submerged jet flow their measured velocity fields are hardly comparable to the presently investigated free surface flow. Stevens & Webb (1993) measured free surface liquid jets impinging on rotating disks, but they had extreme difficulties to resolve experimentally the conditions near the wall, so that the accuracy of their results is rather doubtful. Therefore, most experimental studies measured only the radial profiles of the film thickness or depth-averaged radial velocities, such as Charwat *et al.* (1972), Lenewit *et al.* (2003), Leshev & Peev (2003). A comprehensive detailed description of the flow field inside the liquid in the impingement regions is still missing. The present work intends to shed some light on the flow in the zone.

1.2 Objectives

The present work attempts to investigate the influence of the inflow conditions on the film flow in the region near the impingement of the liquid performing numerical simulations of the flow. In particular, the focus is on the influence of the vertical distance between the nozzle of the dispenser and the disk (termed "nozzle-to-disk distance") as well as the influence of the laminar or turbulent inflow. A series of numerical simulations is carried out assuming different nozzle-to-disk distances for the vertical inflow conditions.

The liquid flow rate and the rotational speed are varied for the individual simulation cases in order to cover a practically relevant range of operating conditions of the real wet spin-process. The effect of the centrifugal forces induced by the rotation at different rotational speeds on the turbulence, which comes into play at sufficiently high (supercritical) flow rates, shall be analyzed. The investigation of the turbulence in the area of impingement is particularly interesting, because there are only scarce previous works which are addressed this issue.

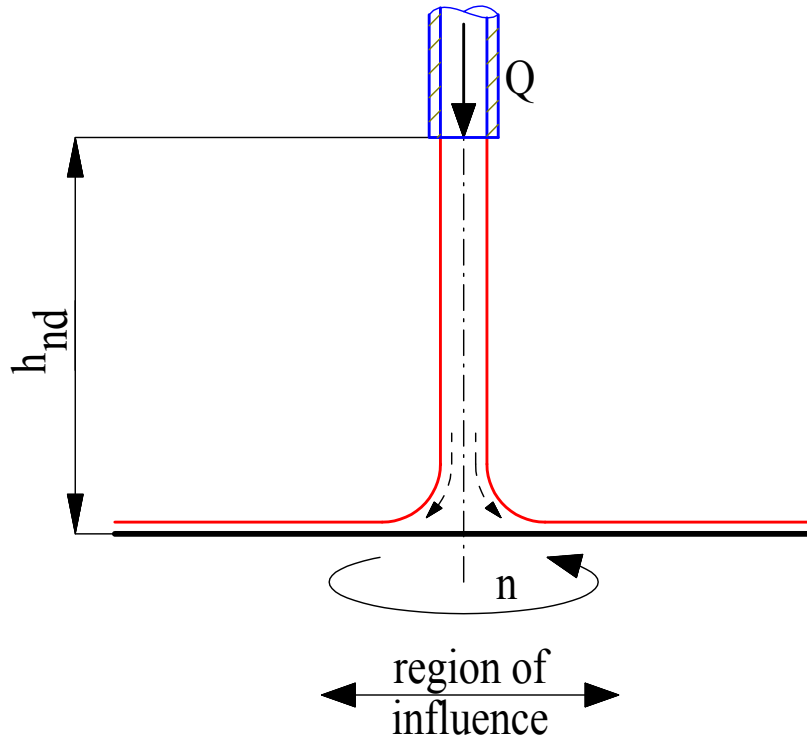


Figure 4: Sketch of the impinging jet on the rotating disk with the varying parameters Q , h_{nd} and n .

Central impingement is prescribed in all cases, so that the flow can be assumed as axisymmetric, which allows for a spatially two-dimensional simulation. Furthermore, the comparison between numerical solutions of ANSYS FLUENT with the previous approximation is of interest. In summary the

present work is intended to extend our knowledge on the following points:

- influence of inflow conditions (Q, h_{nd}) on liquid flow near the impingement,
- the effect of the rotational speed n ,
- the radial extension of the region, where the influence of the inflow conditions is significant. It is termed "region of influence" as shown in Figure 4.

2 Numerical Simulation

This section describes the mathematical formulation of the governing set of equations of the problem. The following subsections discuss in particular the basic equations of the considered flow configuration, the multiphase model, the turbulence model and the numerical solution. The simulation software ANSYS Fluent is used for the numerical flow simulations. Accordingly, the Fluent 6.3 Users Guide (2006) is the base of the here presented material.

2.1 Basic equations of fluid mechanics

The basic equations of the fluid mechanics are the conservation equations of

- mass (continuity equation),
- momentum and
- energy.

The presently considered flow is assumed isothermal, and therefore the energy equation can be disregarded. The general form of the governing equations of motion which are valid for incompressible as well as compressible flows can be written as

$$\frac{\partial \rho}{\partial t} + \nabla \cdot (\rho \vec{v}) = 0 \quad (1)$$

for the continuity, and

$$\frac{\partial (\vec{v}\rho)}{\partial t} + \nabla \cdot (\rho \vec{v}\vec{v}) = \nabla p + \nabla \cdot \mu \left[\nabla \vec{v} + (\nabla \vec{v})^T - \frac{2}{3} (\nabla \cdot \vec{v}) \right] + \vec{F}^B \quad (2)$$

for the momentum. They are also called the Navier-Stokes equations. Assuming a cylindrical coordinate system the velocity vector reads

$$\vec{v} = \begin{pmatrix} v_r \\ v_\phi \\ v_z \end{pmatrix}. \quad (3)$$

The vector \vec{F}^B represents the body force per unit mass.

Assuming further axially symmetric flow the continuity equation can be rewritten as follows

$$\frac{\partial \rho}{\partial t} + \frac{\partial}{\partial z} (\rho v_z) + \frac{\partial}{\partial r} (\rho v_r) + \frac{\rho v_r}{r} = 0, \quad (4)$$

and the axial and the radial momentum equations become

$$\begin{aligned} \frac{\partial}{\partial t} (\rho v_z) + \frac{1}{r} \frac{\partial}{\partial z} (r \rho v_z v_z) + \frac{1}{r} \frac{\partial}{\partial r} (r \rho v_r v_z) = & -\frac{\partial p}{\partial z} + \frac{1}{r} \frac{\partial}{\partial z} \left[r \mu \left(2 \frac{\partial v_z}{\partial z} - \frac{2}{3} (\nabla \cdot \vec{v}) \right) \right] \\ & + \frac{1}{r} \frac{\partial}{\partial r} \left[r \mu \left(\frac{\partial v_z}{\partial r} + \frac{\partial v_r}{\partial z} \right) \right] + F_z, \end{aligned} \quad (5)$$

$$\begin{aligned} \frac{\partial}{\partial t} (\rho v_r) + \frac{1}{r} \frac{\partial}{\partial z} (r \rho v_z v_r) + \frac{1}{r} \frac{\partial}{\partial r} (r \rho v_r v_r) = & -\frac{\partial p}{\partial r} + \frac{1}{r} \frac{\partial}{\partial z} \left[r \mu \left(\frac{\partial v_r}{\partial z} - \frac{\partial v_z}{\partial r} \right) \right] \\ & + \frac{1}{r} \frac{\partial}{\partial r} \left[r \mu \left(2 \frac{\partial v_r}{\partial r} - \frac{2}{3} (\nabla \cdot \vec{v}) \right) \right] - 2 \mu \frac{v_r}{r^2} + \frac{2}{3} \frac{\mu}{r} (\nabla \cdot \vec{v}) + \rho \frac{v_z^2}{r} + F_r, \end{aligned} \quad (6)$$

where

$$\nabla \cdot \vec{v} = \frac{\partial v_z}{\partial z} + \frac{\partial v_r}{\partial r} + \frac{v_r}{r}. \quad (7)$$

The tangential momentum equation is not relevant due to the assumed axisymmetry of the flow.

2.2 Multiphase model

The present work considers a flow with an interface between the liquid and the ambient gaseous phase. This basically requires the use of a multiphase model. For this kind of time-dependent two-phase flow, the volume of fluid (VOF) model is very suitable. The VOF model was developed by Hirt & Nichols (1981) and is designed for two or more immiscible fluids, where one mo-

momentum equations is shared by the different fluids. In the VOF model each computational cell is associated with a certain volume fraction. Depending on the volume fraction the cells are shared by the individual phases providing volume-averaged values for all material properties and flow variables. In two-phase flow the volume fraction α_q essentially distinguishes in three regions.

- $\alpha_q = 0$: The cell contains only gaseous phase.
- $\alpha_q = 1$: The cell contains only liquid.
- $0 < \alpha_q < 1$: The cell contains an interface between the liquid and the gaseous phase.

The index $q = 1$ refers to the liquid phase. Assigning the indices $q = 1$ to the liquid and $q = 2$ to the gas the indicator functions must fulfill

$$\sum_{q=1}^2 \alpha_q = 1, \tag{8}$$

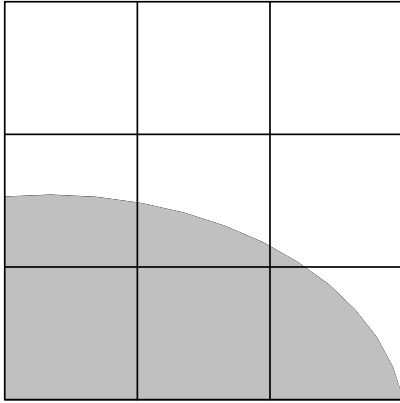


Figure 5: True interface on a computational grid

0	0	0
0.5	0.3	0.1
1	1	0.7

Figure 6: Volume of fluid fractions with values of α_q for each cell

Figure 5 exemplary shows a true interface between two different fluids and Figure 6 shows the corresponding values of the volume fraction of the (gray shaded) primary phase α_1 in each computational cell. Dealing with two-phase flow of two incompressible phases, with $\alpha = \alpha_1$ referring to the liquid and $1 - \alpha = \alpha_2$, referring to the gas the evolution of the liquid phase can be tracked by the transport equation

$$\frac{\partial}{\partial t} (\alpha) + \nabla \cdot (\alpha \vec{v}_q) = 0. \quad (9)$$

After a time discretization using an explicit scheme this equation can be written as

$$\frac{\alpha^{n+1} - \alpha^n}{\Delta t} V + \sum_f (U_f^n \alpha_f^n) = 0, \quad (10)$$

where the index n stands for the time step, α_f for the value of the liquid volume fraction at the face f of each computational cell, V for the volume of the cell, and U_f for the volume flux across the face f . Assuming constant densities (ρ_l, ρ_g) and viscosities (μ_l, μ_g) for the liquid and the gaseous phase the density and the viscosity in each cell are obtained as

$$\rho = \alpha \rho_l + (1 - \alpha) \rho_g \quad (11)$$

and

$$\mu = \alpha \mu_l + (1 - \alpha) \mu_g. \quad (12)$$

The maximum allowed size of the time step Δt depends of the Courant number, which should be smaller than 1 for a stable simulation. This is laid down by the Courant-Friedrich-Levy condition written as

$$CFL = \frac{v_{fluid} \Delta t}{\Delta x_{cell}} \leq 1. \quad (13)$$

In the present work a time step has been set based on the CFL-condition (13) with a maximum Courant number of 0.25 to ensure a stable simulation.

The VOF model also includes the effect of the surface tension σ . In this work the surface tension was set to the constant value $\sigma = 0.072 \frac{N}{m}$. The surface tension force is introduced into the momentum equation using the continuum surface force (CSF) approach proposed by Brackbill *et al.* (1992). This approach incorporates the effect of the surface tension, which is basically a surface force due to the discontinuous pressure across the gas-liquid interface, in terms of a volumetric force, which is added to the momentum equations. The pressure drop across the gas-liquid interface is described with

$$p_2 - p_1 = \sigma \left(\frac{1}{R_1} + \frac{1}{R_2} \right), \quad (14)$$

where p_1 and p_2 are the pressures on either side of the interface and R_1 and R_2 are the principle radii of curvature of the interface. The finally obtained volumetric force is written as

$$F_{vol} = \sigma \frac{\rho \kappa \nabla \alpha}{\frac{1}{2}(\rho_l + \rho_g)}. \quad (15)$$

The local curvature of the interface κ is defined in terms of the divergence of the unit normal vector written as

$$\kappa = \nabla \cdot \frac{\vec{n}}{|\vec{n}|}, \quad (16)$$

where the normal vector is obtained as

$$\vec{n} = \nabla \alpha_q. \quad (17)$$

The density occurring in the nominator of Eq. (15) is the volume-averaged density ρ computed from Eq. (11).

If non-wetted (dry) regions appear, the dynamics at the three-phase contact line has to be modelled as well. In the present VOF model this is done by including a so called wall adhesion model, which is essentially based on the introduction of a contact angle Θ_w . As it is shown in Figure 7, Θ_w is defined as the angle between the wall and the tangent on the interface at the wall.

According to Young's equation this angle depends on the surface tension between the solid and the liquid σ_{sl} , the surface tension between the solid and the gas σ_{sg} , and the surface tension between the liquid and the gas σ , written as

$$\cos \Theta_w = \frac{\sigma_{sg} - \sigma_{sl}}{\sigma}. \quad (18)$$

In this work a value $\Theta_w = 20^\circ$ is used for all cases.

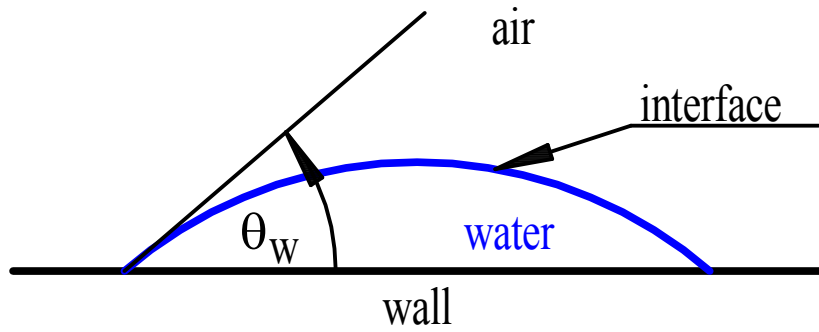


Figure 7: Contact angle at the triple point between the air, water and solid substrate

The prescribed contact angle is implemented as a dynamic wall boundary condition, where it is used to determinate the unit normal vector on the interface at the wall written as

$$\hat{n} = \hat{n}_w \cos(\Theta_w) + \hat{t}_w \sin(\Theta_w) \quad (19)$$

with \hat{n}_w and \hat{t}_w being the unit vectors normal and tangential to the wall, respectively. The unit normal vector obtained from Eq. (19) is used in Eq. (16) to determine the curvature for the first near-wall cell. The wall adhesion model is only important, if dry areas exist, e.g., when initializing the simulation with a dry non-wetted disk, or, in the case of film rupture leading locally to dewetted zones. In a stably running numerical simulation of a continuously wetted disk the contact angle has no relevance.

2.3 Turbulence Models

The key parameter for the stability of a flow with respect to the transition to turbulence is the Reynolds number. It is defined as the ratio of the inertial to the viscous forces and can be written as follows

$$Re = \frac{UL}{\nu}, \quad (20)$$

where U is a relevant velocity scale, L is a characteristic length scale, and ν is the kinematic viscosity. Beyond a certain critical value Re_{crit} the flow becomes unstable and undergoes a transition into the turbulent regime. This regime is in contrast to the laminar flow associated with strongly irregular and intense fluctuations of the flow quantities. Performing a direct numerical simulation (DNS) the highly irregular fluctuating motion has to be fully resolved in space and time, so that no turbulence model is needed. However, due to the high resolution requirements the computational costs of DNS are unacceptably high for most technically relevant turbulent flow configurations. Therefore, a turbulence model has to be applied in most cases.

The turbulence models are typically based on the Reynolds decomposition, which decomposes the instantaneous flow quantities into the mean and the fluctuating components written as

$$v_z = \bar{v}_z + v'_z, v_r = \bar{v}_r + v'_r, v_\phi = \bar{v}_\phi + v'_\phi, p = \bar{p} + p'. \quad (21)$$

Figure 8 exemplarily shows the temporal fluctuation of an arbitrary flow quantity ϕ in a turbulent flow field at some position.

Introducing the decomposition defined in Eq. (21) into the equations of motion yields the so called Reynolds Averaged Navier Stokes (RANS) equations. Assuming a cylindrical coordinate system the RANS-type continuity and momentum equations are written as

$$\frac{\partial \bar{v}_r}{\partial r} + \frac{\bar{v}_r}{r} + \frac{1}{r} \frac{\partial \bar{v}_\phi}{\partial \phi} + \frac{\partial \bar{v}_z}{\partial z} = 0, \quad (22)$$

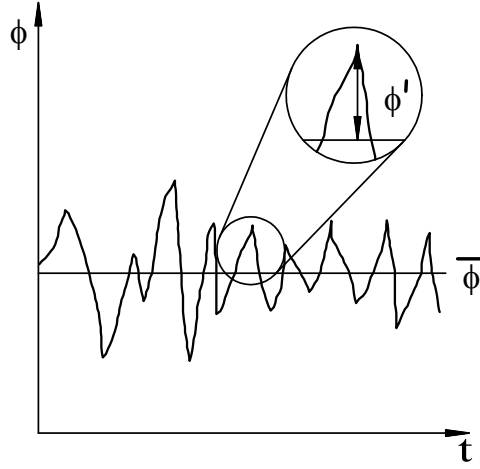


Figure 8: Temporal fluctuation of an arbitrary quantity ϕ

$$\begin{aligned}
 & \rho \left(\frac{\partial \bar{v}_r}{\partial t} + \bar{v}_r \frac{\partial \bar{v}_r}{\partial r} + \frac{\bar{v}_\phi}{r} \frac{\partial \bar{v}_r}{\partial \phi} - \frac{\bar{v}_\phi^2}{r} + \bar{v}_z \frac{\partial \bar{v}_r}{\partial z} \right) = \\
 & -\frac{\partial \bar{p}}{\partial r} + \mu \left(\frac{\partial^2 \bar{v}_r}{\partial r^2} + \frac{1}{r} \frac{\partial \bar{v}_r}{\partial r} - \frac{\bar{v}_r}{r^2} + \frac{1}{r^2} \frac{\partial^2 \bar{v}_r}{\partial \phi^2} - \frac{2}{r^2} \frac{\partial \bar{v}_\phi}{\partial \phi} + \frac{\partial^2 \bar{v}_r}{\partial z^2} \right) \\
 & -\rho \left(\frac{1}{r} \frac{\partial r \overline{v'_r v'_r}}{\partial r} + \frac{1}{r} \frac{\partial \overline{v'_r v'_\phi}}{\partial \phi} - \frac{\overline{v'^2_\phi}}{r} + \frac{\partial \overline{v'_r v'_z}}{\partial z} \right), \quad (23)
 \end{aligned}$$

$$\begin{aligned}
 & \rho \left(\frac{\partial \bar{v}_z}{\partial t} + \bar{v}_r \frac{\partial \bar{v}_z}{\partial r} + \frac{v_\phi}{r} \frac{\partial \bar{v}_z}{\partial \phi} + \bar{v}_z \frac{\partial \bar{v}_z}{\partial z} \right) = \\
 & -\frac{\partial \bar{p}}{\partial z} + \mu \left(\frac{\partial^2 \bar{v}_z}{\partial r^2} + \frac{1}{r} \frac{\partial \bar{v}_z}{\partial r} + \frac{1}{r^2} \frac{\partial^2 \bar{v}_z}{\partial \phi^2} + \frac{\partial^2 \bar{v}_z}{\partial z^2} \right) \\
 & -\rho \left(\frac{1}{r} \frac{\partial r \overline{v'_r v'_z}}{\partial r} + \frac{1}{r} \frac{\partial \overline{v'_\phi v'_z}}{\partial \phi} + \frac{\partial \overline{v'_z v'_z}}{\partial z} \right). \quad (24)
 \end{aligned}$$

The Reynolds stresses appearing as unclosed terms on the RHS of the momentum equations must be modeled in order to close the set of equations. There is variety of turbulence models available, but none of them can be considered as the most suitable for all kinds of problems. It is therefore useful to look at results obtained for some reference cases in order to choose

an appropriate turbulence model. The selection essentially depends on several aspects, such as the established practice for a specific class of problems, the level of accuracy required, the available computational resources, and the amount of computational time available for the simulation. Most of the currently used models fall into the eddy-viscosity models, which follow the Boussinesq-Ansatz. This approach models the effect of the turbulent fluctuating motion in terms of a turbulent viscosity μ_t . The turbulent viscosity is added to its molecular counterpart of the fluid μ_l , and the resulting total, or “effective”, viscosity

$$\mu_{tot} = \mu_l + \mu_t \quad (25)$$

is used in the equations of motion to compute the viscous stress terms. Laminar flow is evidently associated with the turbulent contribution $\mu_t = 0$. The Boussinesq-Ansatz basically postulates that the turbulent stress tensor can be written as

$$-\rho \overline{u'_i u'_j} = \mu_t \left(\frac{\partial \bar{u}_i}{\partial x_j} + \frac{\partial \bar{u}_j}{\partial x_i} \right) - \frac{2}{3} \left(\rho k + \mu_t \frac{\partial \bar{u}_k}{\partial x_k} \right) \delta_{ij}. \quad (26)$$

Two well established approaches are widely used to compute the eddy-viscosity μ_t , the k - ϵ , and the k - ω model. The first solves two additional transport equations for the turbulence kinetic energy k and the dissipation rate ϵ to obtain the eddy-viscosity as

$$\mu_t = \rho C_\mu \frac{k^2}{\epsilon}. \quad (27)$$

The latter model solves two transport equations for k , and for the specific dissipation rate

$$\omega = \frac{\epsilon}{k} \quad (28)$$

to compute the eddy-viscosity as

$$\mu_t = C_\rho \frac{k}{\omega}. \quad (29)$$

The specification of the model parameters occurring in Eqs. (27) and (29)

varies between the different particular kinds of models, which have been proposed within the two groups. The turbulent kinetic energy is defined as

$$k = \frac{\overline{u'_i u'_i}}{2}. \quad (30)$$

The turbulence dissipation rate ϵ is related to the turbulent mixing length by

$$\epsilon = \frac{C_\mu^{3/4} k^{3/2}}{l_m}. \quad (31)$$

In the present work two special kinds of k - ϵ and k - ω model are applied the so called realizable k - ϵ model, and the SST k - ω .

2.3.1 Realizable k - ϵ

Basically there have been established three different types of k - ϵ models, which solve the transport equations for the kinetic energy k and the turbulent dissipation rate ϵ , from which the eddy-viscosity is computed. These are

- the standard k - ϵ ,
- the RNG (renormalization group theory) k - ϵ ,
- realizable k - ϵ model.

The major difference in these models are the methods of calculating turbulent viscosity, the Prandtl numbers governing the turbulent diffusion of k and ϵ , and the generation and destruction terms in the ϵ equation. The k - ϵ models belong to the two-equations models in which the solution of two transport equations determines the turbulent velocity and the turbulent length scale. Using the Boussinesq-Ansatz for computing the Reynolds stress tensor may lead to inaccurate or even non-physical predictions for the normal stresses in highly strained regions. To avoid these deficits the realizable k - ϵ model was developed by Shih *et al.* (1995). The version of this model as it is implemented in ANSYS-Fluent is used and tested in the present work.

The two main differences between the realizable k - ϵ and the standard k - ϵ model are a modified formulation for the turbulent viscosity and for the transport equation of the dissipation rate ϵ . The term "realizable" means that the model satisfies certain mathematical constraints on the Reynold stresses to ensure that the predicted normal stresses are consistent with the physics of turbulent flows. According to the Boussinesq-Ansatz the normal stress component is obtained as

$$\overline{u'^2} = \frac{2}{3}k - 2\frac{\mu_t}{\rho} \frac{\partial \bar{u}}{\partial x}. \quad (32)$$

Substituting the expression for μ_t given by Eq. (27) leads to a negative normal stress, if

$$\frac{k}{\epsilon} \frac{\partial \bar{u}}{\partial x} > \frac{1}{3C_\mu} = 3.7 \quad (33)$$

with the C_μ assumed as 0.09. The realizable k - ϵ model enforces the physically required non-negativity of the normal stresses by modifying the parameter C_μ

The transport equation for k is written as

$$\frac{\partial}{\partial t} (\rho k) + \frac{\partial}{\partial x_j} (\rho k \bar{u}_j) = \frac{\partial}{\partial x_j} \left[\left(\mu + \frac{\mu_t}{\sigma_k} \right) \frac{\partial k}{\partial x_j} \right] + G_k - \rho \epsilon + S_k \quad (34)$$

which is the same as in the standard k - ϵ model, while a modified transport equation is used for ϵ . It is written as

$$\frac{\partial}{\partial t} (\rho \epsilon) + \frac{\partial}{\partial x_j} (\rho \epsilon \bar{u}_j) = \frac{\partial}{\partial x_j} \left[\left(\mu + \frac{\mu_t}{\sigma_\epsilon} \right) \frac{\partial \epsilon}{\partial x_j} \right] + \rho C_1 S \epsilon - \rho C_2 \frac{\epsilon^2}{k + \sqrt{\nu \epsilon}} + S_\epsilon \quad (35)$$

where

$$C_1 = \max \left[0.43, \frac{S_\epsilon^k}{S_\epsilon^k + 5} \right], \quad C_2 = 1.9, \quad \sigma_k = 1.0, \quad \sigma_\epsilon = 1.0. \quad (36)$$

G_k is the production of the turbulence kinetic energy, and it is defined as

$$G_k = \mu_t S^2, \quad (37)$$

where S is the modulus of the mean rate-of-strain tensor which is defined as follows

$$S \equiv \sqrt{2S_{ij}S_{ji}}, \text{ with } S_{ij} = \frac{1}{2} \left(\frac{\partial \bar{u}_j}{\partial x_i} + \frac{\partial \bar{u}_i}{\partial x_j} \right). \quad (38)$$

The turbulent viscosity in the realizable k - ϵ is defined by the same expression as in the standard k - ϵ model shown in Eq. (27), but using a non-constant parameter C_μ . In the realizable k - ϵ this coefficient is computed from

$$C_\mu = \frac{1}{A_0 + A_S \frac{kU^*}{\epsilon}}, \quad (39)$$

where

$$U^* \equiv \sqrt{S_{ij}S_{ij} + \tilde{\Omega}_{ij}\tilde{\Omega}_{ij}} \quad (40)$$

and

$$\tilde{\Omega}_{ij} = \overline{\Omega_{ij}} - \epsilon_{ijk}\omega_k \quad (41)$$

where $\overline{\Omega_{ij}}$ is the mean rate-of rotation tensor defined as

$$\overline{\Omega_{ij}} = \frac{1}{2} \left(\frac{\partial \bar{u}_j}{\partial x_i} - \frac{\partial \bar{u}_i}{\partial x_j} \right) \quad (42)$$

viewed in a rotating frame with the angular velocity ω_k . The model constants are computed from

$$A_0 = 4.04, \quad A_S = \sqrt{6} \cos \phi, \quad (43)$$

where

$$\phi = \frac{1}{3} \cos^{-1} \left(\sqrt{6}W \right), \quad W = \frac{S_{ij}S_{jk}S_{ki}}{\tilde{S}^3}, \quad \tilde{S} = \sqrt{S_{ij}S_{ij}}. \quad (44)$$

The k - ϵ models are primarily developed and valid for turbulent flows far away from walls. Very close to the wall, viscous damping reduces the tangential velocity fluctuations, while kinematic blocking reduces the normal fluctuations. Toward the outer part of the near wall region, the turbulence is rapidly increased by the production of turbulence kinetic energy due to the large gradient in the mean velocity. Accounting for the reduction of the turbulent motion near the walls to make the k - ϵ model valid for the near wall region ANSYS FLUENT offers several near-wall models which are combined with the k - ϵ model for the computation of the near-wall region. Numerous experiments have shown that the near-wall region can be basically divided into three layers, namely

- a viscous sublayer (laminar)
- a buffer layer or blending region, and
- a fully turbulent region

The typically variation of the mean velocity \bar{u} in these layers can be seen in Figure 9, where the triangle points denote the experimental and the solid lines represent mathematical solutions. The shown non-dimensional variations of

$$u^+ = \frac{\bar{u}}{u_\tau} \quad (45)$$

are plotted over the so called "wall coordinate"

$$y^+ = \rho u_\tau \frac{y}{\mu} \quad (46)$$

where the wall friction velocity

$$u_\tau = \sqrt{\frac{\tau_w}{\rho}} \quad (47)$$

is used as relevant velocity scale. The near wall model which can be used in ANSYS Fluent in combination with the k - ϵ models describes the flow in the buffer and the viscous sublayer. Within these near-wall layers the model

superimposes the velocity as a weighted sum of a laminar (viscous) and a turbulent contribution written as

$$u^+ = e^\Gamma u_{lam}^+ + e^{\frac{1}{\Gamma}} u_{turb}^+. \quad (48)$$

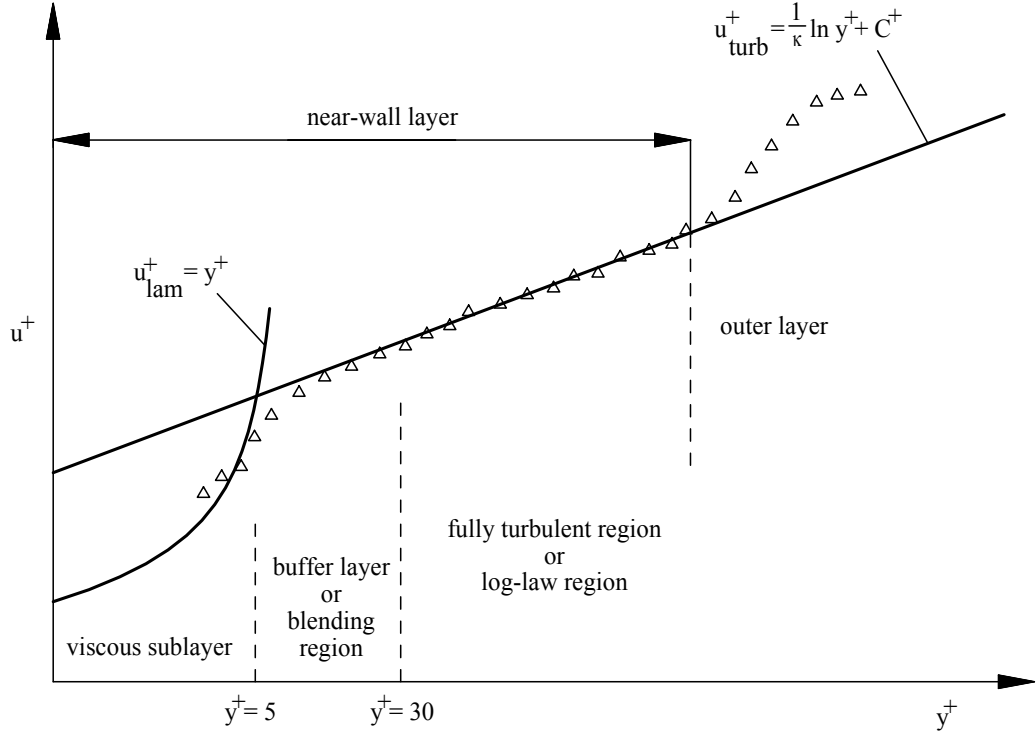


Figure 9: Subdivisions of the near-wall region

This blending follows a proposal of Kader (1981), where the blending function is given by

$$\Gamma = -\frac{a (y^+)^4}{1 + b y^+}, \quad \text{with } a = 0.01 \text{ and } b = 5. \quad (49)$$

The superimposed contributions for the velocities are

$$u_{lam}^+ = y^+ \quad (50)$$

for the laminar part, and

$$u_{turb}^+ = \frac{1}{\kappa} \ln y^+ + C^+ \quad (51)$$

for the turbulent part with $C^+ = 5.45$ and $\kappa = 0.41$ (von Kármán constant). It has to be noted that the near wall model based on Eq. (48) requires a very fine resolution of the near-wall region, which implies that the wall-coordinate of the first grid point near the wall should be $y^+ \approx 1$ or less.

2.3.2 SST k - ω

The shear-stress transport (SST) k - ω model was developed by Menter (1994) to combine the advantage of the standard k - ω model in the near-wall region and the advantage of the k - ϵ model in the far field. For combination of the advantages of each model a blending function is applied to superimpose the standard k - ϵ model and a transformed k - ω model. This particular feature makes the SST k - ω model very reliable for many kinds of flow. A big advantage of this model is that no other model is necessary for resolving the near-wall region. The SST k - ω model is also a two-equation model. Its formulation is similar to the standard k - ω model, and it is written as

$$\frac{\partial}{\partial t} (\rho k) + \frac{\partial}{\partial x_i} (\rho k \bar{u}_i) = \frac{\partial}{\partial x_j} \left(\Gamma_k \frac{\partial k}{\partial x_j} \right) + G_k - Y_k + S_k \quad (52)$$

and

$$\frac{\partial}{\partial t} (\rho \omega) + \frac{\partial}{\partial x_i} (\rho \omega \bar{u}_i) = \frac{\partial}{\partial x_j} \left(\Gamma_\omega \frac{\partial \omega}{\partial x_j} \right) + G_\omega - Y_\omega + D_\omega + S_\omega, \quad (53)$$

where G_k and G_ω represent the production, Y_k and Y_ω the dissipation, Γ_k and Γ_ω the diffusion and D_ω the cross-diffusion. The cross-diffusion term is due to the blending between k - ω and the k - ϵ model. As such, it arises from the transformation of the transport equation for k and ϵ into to corresponding transport equations for k and ω . Γ_k and Γ_ω are the effective diffusivities for

k and ω , and are given by

$$\Gamma_k = \mu + \frac{\mu_t}{\sigma_k}, \quad (54)$$

$$\Gamma_\omega = \mu + \frac{\mu_t}{\sigma_\omega}, \quad (55)$$

respectively. The turbulent viscosity μ_t is computed as follows

$$\mu_t = \frac{\rho k}{\omega} \frac{1}{\max\left[\frac{1}{\alpha^*}, \frac{SF_2}{a_1\omega}\right]}. \quad (56)$$

The turbulent Prandtl numbers for k and ω are

$$\sigma_k = \frac{1}{F_1/\sigma_{k,1} + (1 - F_1)/\sigma_{k,2}}, \quad (57)$$

$$\sigma_\omega = \frac{1}{F_1/\sigma_{\omega,1} + (1 - F_1)/\sigma_{\omega,2}}, \quad (58)$$

respectively. The coefficient α^* is introduced for a low Reynolds number correction and is given by

$$\alpha^* = \alpha_\infty^* \left(\frac{\alpha_0^* + Re_t/R_k}{1 + Re_t/R_k} \right), \quad (59)$$

where

$$Re_t = \frac{\rho k}{\mu\omega}, \quad R_k = 6, \quad \alpha_0^* = \frac{0.072}{3}. \quad (60)$$

The blending functions F_1 and F_2 are defined as follows:

$$F_1 = \tanh(\Phi_1^4) \quad (61)$$

$$\Phi_1 = \min \left[\max \left(\frac{\sqrt{k}}{\beta_\infty^* \omega y}, \frac{500\mu}{\rho y^2 \omega} \right), \frac{4\rho k}{\sigma_{\omega,2} D_\omega^+ y^2} \right] \quad (62)$$

$$D_\omega^+ = \max \left[2\rho \frac{1}{\sigma_{\omega,2}} \frac{1}{\omega} \frac{\partial k}{\partial x_j} \frac{\partial \omega}{\partial x_j}, 10^{-10} \right] \quad (63)$$

$$F_2 = \tanh(\Phi_2^2) \quad (64)$$

$$\Phi_2 = \max \left[2 \frac{\sqrt{k}}{\beta_\infty^* \omega y}, \frac{500\mu}{\rho y^2 \omega} \right]. \quad (65)$$

Herein, D_ω^+ is the positive portion of the cross-diffusion term, which is given by

$$D_\omega = 2(1 - F_1) \rho \bar{\sigma}_{\omega,2} \frac{1}{\omega} \frac{\partial k}{\partial x_j} \frac{\partial \omega}{\partial x_j}. \quad (66)$$

The production terms can be written as

$$G_k = \min \left(-\overline{\rho u'_i u'_j} \frac{\partial \bar{u}_j}{\partial x_i}, 10\rho\beta^* k\omega \right), \quad (67)$$

where

$$\beta^* = \beta_\infty^* \left(\frac{4/15 + (Re_t/8)^4}{1 + (Re_t/8)^2} \right), \quad (68)$$

and

$$G_\omega = \frac{\alpha}{\nu_t} \left(-\overline{\rho u'_i u'_j} \frac{\partial \bar{u}_j}{\partial x_i} \right), \quad (69)$$

where

$$\alpha = \frac{\alpha_\infty}{\alpha^*} \left(\frac{\alpha_0 + Re_t/R_\omega}{1 + Re_t/R_\omega} \right) \quad (70)$$

with R_ω is 2.95. The constant α_∞ is defined as

$$\alpha_\infty = F_1 \alpha_{\infty,1} + (1 - F_1) \alpha_{\infty,2}, \quad (71)$$

where

$$\alpha_{\infty,1} = \frac{\beta_{i,1}}{\beta_\infty^*} - \frac{\kappa^2}{\sigma_{\omega,1} \sqrt{\beta_\infty^*}}, \quad (72)$$

$$\alpha_{\infty,2} = \frac{\beta_{i,2}}{\beta_{\infty}^*} - \frac{\kappa^2}{\sigma_{\omega,2}\sqrt{\beta_{\infty}^*}}. \quad (73)$$

Y_k and Y_{ω} are the dissipation terms and are computed similar to the standard k - ω model. They can be written as

$$Y_k = \rho\beta^*k\omega \quad (74)$$

and

$$Y_{\omega} = \rho\beta k\omega^2, \quad (75)$$

where

$$\beta = \beta_i = F_1\beta_{i,1} + (1 - F_1)\beta_{i,2}. \quad (76)$$

The model constants involved in the formulation above are

$$\begin{aligned} \sigma_{k,1} = 1.176, \sigma_{k,2} = 2.0, \sigma_{\omega,1} = 1.0, \sigma_{\omega,2} = 1.168, \\ a_1 = 0.31, \beta_{\infty}^* = 0.09, \beta_{i,1} = 0.075, \beta_{i,2} = 0.075, \kappa = 0.41. \end{aligned} \quad (77)$$

The wall boundary conditions for the SST k - ω model are similar to the enhanced wall treatment for the k - ϵ model, in that a blending function between a viscous and turbulent solution is used for the computation of ω^+ near the wall analogously to Eq. (48). In ANSYS FLUENT the value of the specific dissipation ω at the wall is defined as follows

$$\omega_w = \frac{\rho(u^*)^2}{\mu}\omega^+ \quad (78)$$

with the asymptotic value

$$\omega^+ = \min\left(\omega_w^+, \frac{6}{\beta_i(y^+)^2}\right) \quad (79)$$

in the laminar sublayer, where

$$\omega_w^+ = \begin{cases} \left(\frac{50}{k_s^+}\right)^2 & k_s^+ < 25 \\ \frac{100}{k_s^+} & k_s^+ \geq 25 \end{cases} \quad (80)$$

with

$$k_s^+ = \max\left(1.0, \frac{\rho k_s u^*}{\mu}\right) \quad (81)$$

and k_s is the roughness height. The occurring wall friction velocity is defined as shown in Eq. (47). In the turbulent region ω^+ is obtained as

$$\omega^+ = \frac{1}{\sqrt{\beta_\infty^*}} \frac{du_{turb}^+}{dy^+}, \quad (82)$$

$$u^* = C_\mu^{1/4} k^{1/2} \quad (83)$$

which leads to a specific dissipation ω near the wall as

$$\omega = \frac{u^*}{\sqrt{\beta_\infty^*} \kappa y} \quad (84)$$

2.4 Numerical solution

2.4.1 Discretization in space

The Navier-Stokes equations cannot be solved analytically. Therefore, they have to be solved numerically, which means that the continuous space is replaced by a set of discrete points, where a discrete solution is computed for all flow quantities. The discrete numerical solution of flow problems is mostly based on the Finite-Volume method (FV). This popular approach is used by ANSYS-Fluent as well. The FV method basically integrates the governing conservation equations over discrete (finite) control volume, which finally yields discrete balance equations for each volume. This concept is exemplarily sketched in Figure 10,

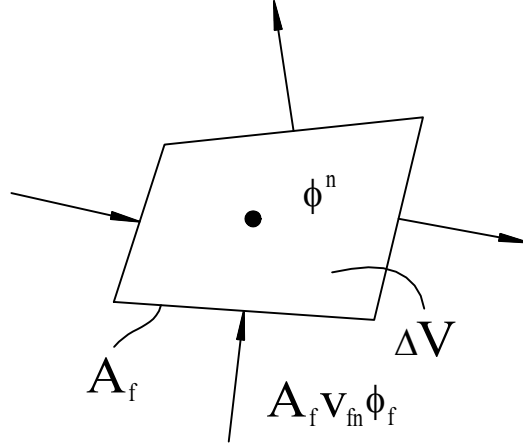


Figure 10: Balance of arbitrary flow quantity ϕ

where the discrete balance equation would read

$$\frac{\phi^{n+1} - \phi^n}{\Delta t} \Delta V + \sum_{f=1}^n (v_{nf} \phi_f A_f) = 0. \quad (85)$$

The accuracy of the finite-volume method strongly depends of a reliable determination of the fluxes across the surface of the control volume (represented by $v_{fn} \phi_f$ in Figure 10). In the present simulations using ANSYS-Fluent these fluxes are computed based on Gauss' divergence theorem applying upwind or central differencing schemes. This standard concept for providing the surface fluxes is, however, not suitable for solving the phase-marker transport equation (Eq. (10)), when dealing with two-phase flow using the VOF method. For the particular case of phase transport several specially designed so called "Interface Capturing Schemes" are available in ANSYS-Fluent, from which the "High Resolution Interface Capturing" (HRIC) (Muzaferija *et al.* (1998)) method was chosen. In the HRIC-scheme, which basically consists of a non-linear blending of upwind and downwind differencing, a normalized volume fraction is defined as

$$\bar{\alpha} = \frac{\alpha_D - \alpha_U}{\alpha_A - \alpha_U}, \quad (86)$$

where A stands for the acceptor cell, D for the donor cell, and U for the

upwind cell.

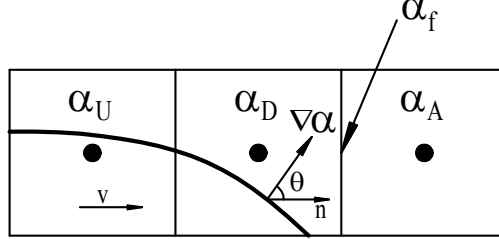


Figure 11: Three neighboring cells containing the interface

Figure 11 shows three neighboring cells containing the interface, where \vec{n} is a face normal unit vector and $\nabla\alpha$ is the gradient of the phase-marker function. In the original version of HRIC the face value determined as

$$\tilde{\alpha}_f = \begin{cases} \bar{\alpha} & \bar{\alpha} < 0 \text{ or } \bar{\alpha} > 1 \\ 2\bar{\alpha} & 0 \leq \bar{\alpha} \leq 0.5 \\ 1 & 0.5 \leq \bar{\alpha} \leq 1 \end{cases} . \quad (87)$$

Setting directly $\alpha_f = \tilde{\alpha}_f$ from Eq. (87) would cause wrinkles in the interface, if the flow is parallel to the interface (Tivert *et al.* (2007)). To avoid this unphysical effect the HRIC scheme is modified based on the angle between the face normal and the interface normal vectors (θ in Figure 11). In contrast to the original HRIC scheme the modified HRIC scheme employs a one-dimensional bounded version of the QUICK scheme to obtain

$$\alpha_f^Q = \begin{cases} \bar{\alpha} & \bar{\alpha} < 0 \text{ or } \bar{\alpha} > 1 \\ \min\left(\tilde{\alpha}_f, \frac{6\bar{\alpha}+3}{8}\right) & 0.5 \leq \bar{\alpha} \leq 1 \end{cases} , \quad (88)$$

which provides a modified value of the face volume fraction given by

$$\tilde{\alpha}_f^* = \tilde{\alpha}_f \sqrt{\cos\theta} + \left(1 - \sqrt{\cos\theta}\right) \alpha_f^Q, \quad (89)$$

where

$$\cos \theta = \frac{\nabla \alpha \cdot \vec{n}}{|\nabla \alpha| |\vec{n}|}. \quad (90)$$

The face volume fraction is finally determined as

$$\alpha_f = \tilde{\alpha}_f^* (\alpha_A - \alpha_U) + \alpha_U. \quad (91)$$

For all the other transport equations (e.g., the momentum or the turbulent kinetic energy, see Tables 1 and 2) a first-order upwind scheme was used for solving the differential equations.

A Least Squares Cell-Based method is used for the discrete computation of the gradients, which occur in the formulation. This method basically assumes that the solution varies linearly. Under this the assumption the gradient of the flow quantity α can be simply obtained as

$$(\nabla \alpha)_{c_0} \Delta r_i = (\alpha_{c_i} - \alpha_{c_0}), \quad (92)$$

where α_{c_i} and α_{c_0} stand for the nodal values which are shown in Figure 12. The Least Squares method has the same accuracy for irregular unstructured meshes as the node-based Green-Gauss method, but is computationally less expensive.

2.4.2 Solver settings

ANSYS FLUENT offers two types of solution algorithm, the density-based and the pressure-based solver. The pressure-based solver, which is applied in the present work is generally used for incompressible flow, while the density-based solver for compressible flow. Solving the momentum equation with the pressure-based solver a predicted flow field is computed in a projection step. This predicted flow field does not satisfy the continuity equation. The satisfaction of the continuity equation is enforced by carrying out a pressure correction, where the Poisson equation is introduced and solved for the pressure at each computational point. In incompressible CFD simulations the solution of the Poisson equation typically consumes most of the total simu-

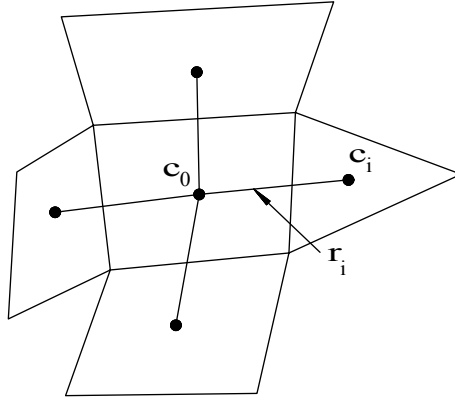


Figure 12: Cell Centroid Evaluation

lation time. Various solution algorithms, which have been developed for this purpose, are implemented in ANSYS-Fluent. In the present simulation the so called Pressure-Implicit with Splitting of Operators (PISO) in combination with the PRESTO! (Pressure Staggering Option) was used.

The presently used solver settings and solution controls are summarized in Table 1.

For the turbulent cases additional settings listed in Table 2 are applied.

2.4.3 Computational domain and discretization

The computational domain used in all the axisymmetric simulation is sketched in Figure 13. Its height at the radial outer boundary above the disk is $h_{out} = 10\text{ mm}$. The radial extension of the disk was set to $R_{max} = 60\text{ mm}$, which is smaller than the radius of the real wafer. Using such a reduced radial domain size was motivated in the first place to reduce the computational costs. Secondly, the focus of the present investigations is on the region near the impingement, and not on the outer radial region. The radial extension of the domain around the incoming vertical liquid jet was set to $R_i = 15\text{ mm}$.

Pressure-Velocity Coupling	
Scheme	PISO
Skewness Correction	1
Neighbor	1
Skewness-Neighbor Coupling	check
Spatial Discretization	
Gradient	Least Squares Cell Based
Pressure	PRESTO!
Momentum	First Order Upwind
Volume Fraction	Modified HRIC
Transient Formulation	First Order Implicit

Table 1: Solver settings and solution controls

Turbulent Kinetic Energy	First Order Upwind
Specific Dissipation Rate	First Order Upwind
Turbulent Dissipation Rate	First Order Upwind

Table 2: Additional settings for the turbulent cases**Automatic grid generator**

A routine for automatic grid generation was programmed and implemented in the meshing software GAMBIT. The total number of grid cells is about 90 000, depending on the nozzle-to-disk distance. The developed meshing routine allows for a fast and efficient generation of different numerical grids varying the geometries of the computational domain as well as local the resolution.

As seen from Figure 14, the grid points are clustered towards the wall to ensure a high spatial resolution of the liquid film flow near the wall. The

number of cells in the radial direction is about 600, which implies an average radial cell size of 0.1 mm . The cell height in the wall normal direction is about $10\ \mu\text{m}$ near the disk.

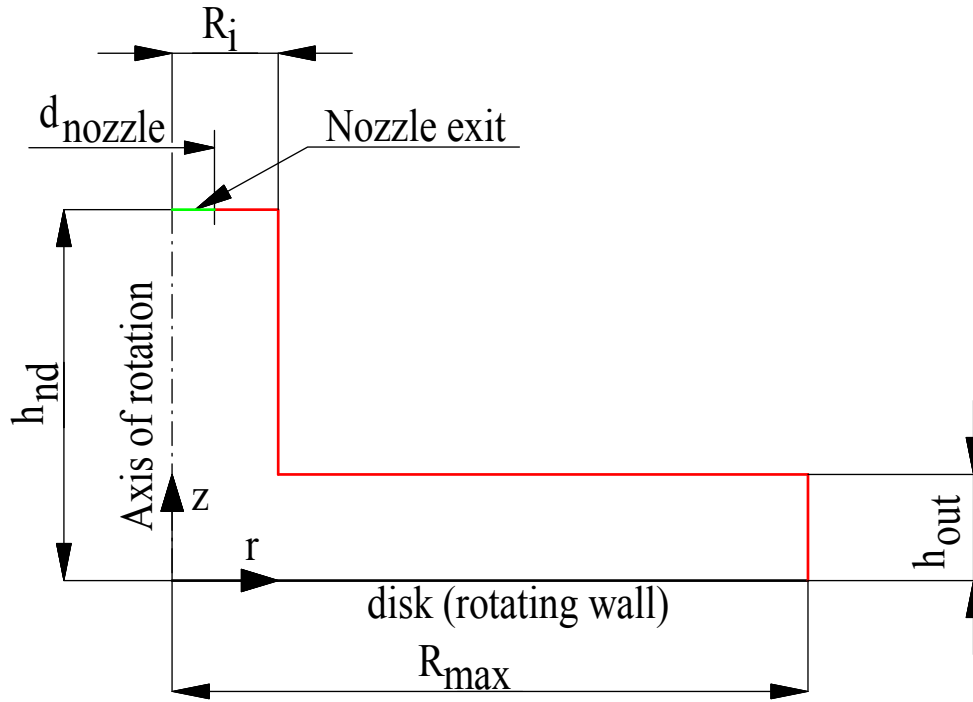


Figure 13: Sketch of the computational domain

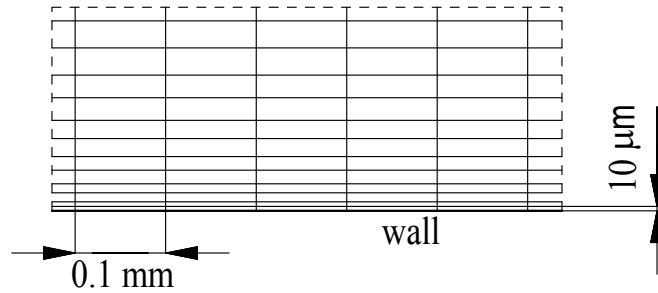


Figure 14: Refined grid near the wall

2.4.4 Boundary conditions

The simulations are carried out in a fixed (non-rotating) frame of reference. The position of the individual boundaries is also indicated in Figure 13, marked by different colors. At the exit of the nozzle a velocity inlet condition with a top-hat profile was used, as shown in Figure 15. The uniform liquid inflow is supposed to come very close to the real inflow conditions owing to the contraction of the flow inside the nozzle immediately upstream. In the case of turbulent inflow the inlet conditions for the turbulent kinetic energy and dissipation rate are prescribed in terms of a turbulent intensity and the hydraulic diameter, which is related to the turbulent length scale. The turbulent intensity was assumed to be 10%, i.e.,

$$\frac{\sqrt{\frac{2}{3}k}}{v_{nozzle}} = 0.1 \quad (93)$$

at the nozzle exit, and the hydraulic diameter was set to the nozzle diameter $d_h = d_{nozzle} = 0.00482 \text{ m}$.

The disk of the bottom of the domain is prescribed as a rotating wall with no-slip conditions. The remaining boundary conditions marked by the red line in Figure 13 are prescribed as a "pressure outlet" conditions imposing a constant ambient pressure. At this outlet boundary the turbulence intensity and hydraulic diameter for the turbulent length scale were set to $I = 0.5\%$

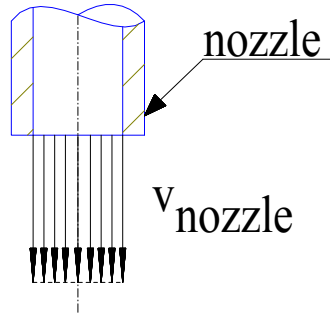


Figure 15: Top-hat velocity profile used as liquid inflow

and $d_h = 0.001\text{ m}$, respectively, to cover the case of reversed, and hence, incoming flow at this boundaries. All boundary conditions applied in the present simulations are summarized in Table 3.

boundary	boundary conditions	additional information
inlet (green)	velocity inlet	top-hat profile
outlet (red)	pressure outlet	ambient pressure
wall (black)	rotating wall	no-slip

Table 3: Boundary condition

3 Approximate Solutions

3.1 Thin Film Equations

The VOF-based numerical simulation described in the previous chapter becomes computationally very costly, especially, when considering the motion of thin liquid films on large solid substrates. The solution of the governing equations applying the thin film approximation represents a computationally much cheaper alternative. This concept which shall be termed in the following the ‘‘Thin Film Equations’’ (TFE) has become a widely used approach for this problem. There are several works in literature, where this concept is applied to the case of film flow on spinning disks (see, e.g., Sisoiev *et al.* (2003), Kim & Kim (2009)). Following these studies appropriate dimensionless are introduced based on the relevant variables characteristic reference scales defined as follows

$$\begin{aligned} u^* &= \frac{u}{\Omega l_0}, v^* = \frac{v}{\Omega l_0}, w^* = \frac{w}{\Omega \delta_0}, \\ r^* &= \frac{r}{l_0}, z^* = \frac{z}{\delta_0}, p^* = \frac{p}{\rho \Omega^2 l_0^2}, t^* = t\Omega, \delta^* = \frac{\delta}{\delta_0}, \end{aligned} \quad (94)$$

involving the length scales δ_0 and l_0 , which are defined by

$$\delta_0 = \left(\frac{\nu_l}{\Omega} \right)^{\frac{1}{2}}, \quad (95)$$

and

$$l_0 = \left(\frac{9Q^2}{4\pi^2 \nu_l \Omega} \right)^{\frac{1}{4}}, \quad (96)$$

respectively. Introducing the definitions above into a cylindrical coordinate system rotating with the speed Ω the dimensionless governing equations for continuity and momentum read

$$\frac{1}{r^*} \frac{\partial}{\partial r^*} (r^* u^*) + \frac{1}{r^*} \frac{\partial v^*}{\partial \theta} + \frac{\partial w^*}{\partial z^*} = 0, \quad (97)$$

$$\begin{aligned} \frac{\partial u^*}{\partial t^*} + u^* \frac{\partial u^*}{\partial r^*} + \frac{v^*}{r^*} \frac{\partial u^*}{\partial \theta} + w^* \frac{\partial u^*}{\partial z^*} - \frac{v^{*2}}{r^*} = -\frac{\partial p^*}{\partial r^*} + r^* + 2v^* + \frac{\partial^2 u^*}{\partial z^{*2}} \\ + \epsilon_0^2 \left(\frac{\partial^2 u^*}{\partial r^{*2}} + \frac{1}{r^*} \frac{\partial u^*}{\partial r^*} + \frac{1}{r^{*2}} \frac{\partial^2 u^*}{\partial \theta^2} - \frac{2}{r^{*2}} \frac{\partial v^*}{\partial \theta} - \frac{u^*}{r^{*2}} \right), \end{aligned} \quad (98)$$

$$\begin{aligned} \frac{\partial v^*}{\partial t^*} + u^* \frac{\partial v^*}{\partial r^*} + \frac{v^*}{r^*} \frac{\partial v^*}{\partial \theta} + w^* \frac{\partial v^*}{\partial z^*} - \frac{u^* v^*}{r^*} = -\frac{1}{r^*} \frac{\partial p^*}{\partial \theta} - 2u^* + \frac{\partial^2 v^*}{\partial z^{*2}} \\ + \epsilon_0^2 \left(\frac{\partial^2 v^*}{\partial r^{*2}} + \frac{1}{r^*} \frac{\partial v^*}{\partial r^*} + \frac{1}{r^{*2}} \frac{\partial^2 v^*}{\partial \theta^2} - \frac{2}{r^{*2}} \frac{\partial u^*}{\partial \theta} - \frac{v^*}{r^{*2}} \right), \end{aligned} \quad (99)$$

$$\begin{aligned} \epsilon_0^2 \left(\frac{\partial w^*}{\partial t^*} + u^* \frac{\partial w^*}{\partial r^*} + \frac{v^*}{r^*} \frac{\partial w^*}{\partial \theta} + w^* \frac{\partial w^*}{\partial z^*} \right) = -\frac{\partial p^*}{\partial z^*} - \epsilon_0 Fr^{-1} + \epsilon_0^2 \frac{\partial^2 w^*}{\partial z^{*2}} \\ + \epsilon_0^4 \left(\frac{\partial^2 w^*}{\partial r^{*2}} + \frac{1}{r^*} \frac{\partial w^*}{\partial r^*} + \frac{1}{r^{*2}} \frac{\partial^2 w^*}{\partial \theta^2} \right), \end{aligned} \quad (100)$$

where the dimensionless parameter $\epsilon_0 = \delta_0/l_0$ and the Froude number $Fr = \Omega^2 l_0/g$ appear. Due to the strong disparity between the vertical and the radial length scales $\delta_0 \ll l_0$, ϵ_0 is very small (thin film), so that all terms preceded by a factor ϵ_0^n with $n \geq 2$ can be neglected yielding the so called thin film approximation written as

$$\frac{1}{r^*} \frac{\partial}{\partial r^*} (r^* u^*) + \frac{1}{r^*} \frac{\partial v^*}{\partial \theta} + \frac{\partial w^*}{\partial z^*} = 0, \quad (101)$$

$$\frac{\partial u^*}{\partial t^*} + u^* \frac{\partial u^*}{\partial r^*} + \frac{v^*}{r^*} \frac{\partial u^*}{\partial \theta} + w^* \frac{\partial u^*}{\partial z^*} - \frac{v^{*2}}{r^*} = -\frac{\partial p^*}{\partial r^*} + r^* + 2v^* + \frac{\partial^2 u^*}{\partial z^{*2}}, \quad (102)$$

$$\frac{\partial v^*}{\partial t^*} + u^* \frac{\partial v^*}{\partial r^*} + \frac{v^*}{r^*} \frac{\partial v^*}{\partial \theta} + w^* \frac{\partial v^*}{\partial z^*} - \frac{u^* v^*}{r^*} = -\frac{1}{r^*} \frac{\partial p^*}{\partial \theta} - 2u^* + \frac{\partial^2 v^*}{\partial z^{*2}}, \quad (103)$$

$$0 = -\frac{\partial p^*}{\partial z^*} - \epsilon_0 Fr^{-1}, \quad (104)$$

The pressure is then obtained by integrating Eq. (104). It reads

$$p^* = p_s^* + \epsilon_0 Fr^{-1} (\delta^* - z^*), \quad (105)$$

where p_s^* is the capillary pressure at the free surface, which is written as

$$p_s^* = -\epsilon_0^3 We \left(\frac{1}{r^*} \frac{\partial}{\partial r^*} \left(r^* \frac{\partial}{\partial r^*} \right) + \frac{1}{r^{*2}} \frac{\partial^2}{\partial \theta^2} \right) \delta^* \quad (106)$$

considering only steady smooth film flow this capillary pressure is neglected due to the small curvature of the liquid surface. The boundary conditions are the no-slip condition at the wall, the stress-free condition and the kinematic boundary condition at the surface, written as

$$z^* = 0 \quad : \quad u^* = v^* = w^* = 0, \quad (107)$$

$$(108)$$

$$z^* = \delta^* \quad : \quad \frac{\partial u^*}{\partial z^*} = 0, \quad \frac{\partial v^*}{\partial z^*} = 0, \quad \frac{\partial w^*}{\partial z^*} = 0, \quad (109)$$

$$\frac{\partial \delta^*}{\partial t} + u^* \frac{\partial \delta^*}{\partial r^*} + \frac{v^*}{r^*} \frac{\partial \delta^*}{\partial \theta} = w^*. \quad (110)$$

The dimensionality of the problem is reduced by solving the depth-averaged representation of the thin film approximation. The depth-averaged formulation is obtained by integrating Eqs. (101)-(104) in the vertical direction from $z^* = 0$ to the film height $z^* = \delta^*$, so that they finally read

$$\frac{1}{r^*} \frac{\partial}{\partial r^*} (r^* \overline{u^* \delta^*}) + \frac{1}{r^*} \frac{\partial}{\partial \theta} (\overline{v^* \delta^*}) = 0, \quad (111)$$

$$\begin{aligned} \frac{1}{r^*} \frac{\partial}{\partial r^*} (r^* \overline{u^{*2} \delta^*}) + \frac{1}{r^*} \frac{\partial}{\partial \theta} (\overline{u^* v^* \delta^*}) - \frac{\overline{v^{*2} \delta^*}}{r^*} = & -\frac{\partial}{\partial r^*} (\overline{p^* \delta^*}) + p_s^* \frac{\partial \delta^*}{\partial r^*} \\ & + r^* \delta^* + 2\overline{v^* \delta^*} - \left. \frac{\partial u^*}{\partial z^*} \right|_{z^*=0}, \end{aligned} \quad (112)$$

$$\begin{aligned} \frac{1}{r^*} \frac{\partial}{\partial r^*} (r^* \overline{u^* v^*} \delta^*) + \frac{1}{r^*} \frac{\partial}{\partial \theta} (\overline{v^{*2}} \delta^*) - \frac{1}{r^*} \overline{u^* v^*} \delta^* = -\frac{1}{r^*} \frac{\partial}{\partial \theta} (\overline{p^*} \delta^*) + p_s^* \frac{1}{r^*} \frac{\partial \delta^*}{\partial \theta} \\ + 2\overline{u^*} \delta^* - \left. \frac{\partial v^*}{\partial z^*} \right|_{z^*=0}, \end{aligned} \quad (113)$$

$$\overline{p^*} = p_s^* + \frac{1}{2} \epsilon_0 Fr^{-1} \delta^*, \quad (114)$$

where the overbars denote the depth-averaged quantities, which are generally defined as

$$\overline{f^*} = \frac{1}{\delta^*} \int_0^{\delta^*} f^* dz^*. \quad (115)$$

The depth-averages of the nonlinear terms as well as the derivatives at the wall occurring in Eqs. (112)-(112) require the assumption of velocity profiles inside the liquid. Sisoiev *et al.* (2003) proposed a quadratic profile for the radial velocity and a quartic profile for the azimuthal velocity written as

$$u^* = u_s^* (2\zeta - \zeta^2), \quad (116)$$

$$v^* = v_s^* \left(\frac{8}{5}\zeta - \frac{4}{5}\zeta^3 + \frac{1}{5}\zeta^4 \right), \quad (117)$$

with

$$\zeta = \frac{z^*}{\delta^*} \quad (118)$$

respectively. The quadratic profile for u^* represents the exact axisymmetric solution in the limit of large radii, where the flow is only governed by the centrifugal and the viscous forces. The quartic profiles for v^* is obtained by integration the azimuthal momentum equations for the axisymmetric case using the quadratic profile for u^* , Eq. (116). The values at the surface are

related to the averages by

$$u_s^* = \frac{3}{2}\overline{u^*}, v_s^* = \frac{25}{16}\overline{v^*}. \quad (119)$$

Using the profile assumption Eqs. (116)-(117) the averaged non-linear terms can be expressed as

$$\overline{u^{*2}} = k_A \overline{u^{*2}}, \overline{u^* v^*} = k_B \overline{u^* v^*}, \overline{v^{*2}} = k_C \overline{v^{*2}}, \quad (120)$$

with

$$k_A = \frac{6}{5}, k_B = \frac{17}{14}, k_C = \frac{155}{126}. \quad (121)$$

The quadratic approximation, Eq. (116) cannot account for the effect of inertial and Coriolis forces, which can lead to less accurate results in the inner radial region near the impingement. Therefore, Kim & Kim (2009) suggested to use a quartic profile written as

$$u^* = u_s^* \left(\frac{8}{5}\zeta - \frac{4}{5}\zeta^3 + \frac{1}{5}\zeta^4 \right) + \frac{\lambda_k \delta^2}{5} \zeta (1 - \zeta)^2 \left(1 - \frac{\zeta}{2} \right). \quad (122)$$

This profile can reflect the effect of inertia and the Coriolis forces, and it satisfies the boundary conditions

$$z^* = 0 : u^* = 0, \quad (123)$$

$$\frac{\partial^2 u^*}{\partial z^{*2}} = -r^* + \frac{\partial p^*}{\partial r^*} \equiv -\lambda_k, \quad (124)$$

$$(125)$$

$$z^* = \delta^* : \frac{\partial^2 u^*}{\partial z^{*2}} = 0. \quad (126)$$

For the here considered axisymmetric flow Kim & Kim (2009) propose the same quartic polynomial for v^* as given in Eq. (117). After some manipulations using quartic profiles assumptions for u^* and v^* the following relations

are obtained

$$u_s^* = \frac{25}{16}\overline{u^*} - \frac{1}{48}\lambda_k\delta^{*2}, \quad (127)$$

$$v_s^* = \frac{25}{16}\overline{v^*}, \quad (128)$$

$$\left. \frac{\partial u^*}{\partial z^*} \right|_{z^*=0} = \frac{5}{2}\frac{\overline{u^*}}{\delta^*} + \frac{1}{6}\lambda_k\delta^*, \quad (129)$$

$$\left. \frac{\partial v^*}{\partial z^*} \right|_{z^*=0} = \frac{5}{2}\frac{\overline{v^*}}{\delta^*}, \quad (130)$$

$$\overline{u^{*2}} = \frac{155}{126}\overline{u^{*2}} - \frac{2}{189}\overline{u^*}\lambda_k\delta^{*2} + \frac{1}{5670}(\lambda_k\delta^{*2})^2, \quad (131)$$

$$\overline{u^*v^*} = \frac{155}{126}\overline{u^*}\overline{v^*} - \frac{1}{189}\overline{v^*}\lambda_k\delta^{*2} + \frac{1}{5670}(\lambda_k\delta^{*2}), \quad (132)$$

$$\overline{v^{*2}} = \frac{155}{126}\overline{v^{*2}}, \quad (133)$$

Substituting the expressions for the non-linear averages, Eqs. (131)-(133), into the momentum equations Eqs. (112)-(113), would lead to a mathematically complex formulation. Therefore, as suggested by Kim & Kim (2009), the simpler expressions, Eq. (120) with Eq. (121), which are based on the quadratic profiles for u^* , are used instead. The quartic profile for u^* is only used for the derivative at the wall given by Eq. (129). Following this concept of Kim & Kim (2009) the resulting depth-averaged continuity and momentum equations for the axisymmetric stationary case read

$$\frac{\partial}{\partial r^*} (r^*\overline{u^*}\delta^*) = 0 \quad (134)$$

$$\begin{aligned} \frac{1}{r^*} \frac{\partial}{\partial r^*} \left(k_A r^* \bar{u}^{*2} \delta^* \right) + \frac{1}{r^*} \frac{\partial}{\partial \theta} \left(k_B \bar{u}^* \bar{v}^* \delta^* \right) - \frac{k_C \bar{v}^{*2} \delta^*}{r^*} \\ = 2\bar{v}^* \delta^* + \frac{5}{6} \left(r^* - \frac{\partial P^*}{\partial r^*} \right) \delta^* - \frac{5 \bar{u}^*}{2 \delta^*}, \end{aligned} \quad (135)$$

$$\frac{1}{r^*} \frac{\partial}{\partial r^*} \left(k_B r^* \bar{u}^* \bar{v}^* \delta^* \right) - \frac{k_B \bar{u}^* \bar{v}^* \delta^*}{r^*} = -2\bar{u}^* \delta^* - \frac{5 \bar{v}^*}{2 \delta^*}, \quad (136)$$

where k_A , k_B , and k_C are given by Eq. (121), and

$$P^* = \epsilon_0 F r^{-1} \delta^* \quad (137)$$

involving the reduced inverse Froude number defined as

$$\tilde{F}^{-1} = \epsilon_0 F r^{-1} = \frac{g \delta_0}{\Omega^2 l_0^2}. \quad (138)$$

The integration of the depth-averaged continuity equation yields

$$r^* \bar{u}^* \delta^* = \frac{1}{3}. \quad (139)$$

The TFE solution for δ^* , \bar{u}^* , and \bar{v}^* is finally computed from the continuity equation (Eq. (139)) together with the following set of coupled ordinary differential equations:

$$\frac{1}{r} \frac{\partial}{\partial r^*} \left(\frac{6}{5} r^* \bar{u}^{*2} \delta^* \right) - \frac{155 \bar{v}^{*2} \delta^*}{126 r^*} = 2\bar{v}^* \delta^* + \frac{5}{6} \left(r^* - \tilde{F}^{-1} \frac{\partial \delta^*}{\partial r^*} \right) - \frac{5 \bar{u}^*}{2 \delta^*} \quad (140)$$

$$\frac{1}{r^*} \frac{\partial}{\partial r^*} \left(\frac{17}{14} r^* \bar{u}^* \bar{v}^* \delta^* \right) + \frac{17 \bar{u}^* \bar{v}^*}{14 r^*} = -2\bar{u}^* \delta^* - \frac{5 \bar{v}^*}{2 \delta^*}. \quad (141)$$

The inner radial boundary condition for the integration of the system (Eqs. (139)-(141)) is obtained from an asymptotic solution valid in the limit of small radii $r \ll 1$, which is written as (Kim & Kim (2009))

$$\delta^* = \frac{C_i}{r^*} + \frac{5r^{*2}}{2k_A}, \quad (142)$$

$$\bar{u}^* = \frac{1}{3(C_i + (5/2k_A)r^{*3})}, \quad (143)$$

$$\bar{v}^* = -\frac{1}{k_B}r^* + \frac{2}{k_B^2 C_i}r^{*4}, \quad (144)$$

evaluated at a given radial position of the inflow boundary, $r^* = r_i^*$. The unknown parameter C_i has to be provided by assuming the film height at the inflow boundary $\delta_i^* = \delta^*|_{r^*=r_i^*}$. In the present work the value for δ_i^* is taken from corresponding CFD results.

With increasing radial distance the TFE solution approaches the so called Nusselt solution, which is obtained from the balance of the centrifugal and the viscous forces. As it was shown by Rauscher *et al.* (1973) the inertial, Coriolis and gravitational forces can be neglected the radial momentum in Eq. (140), so that only the viscous and the centrifugal terms remain. The integration of the so reduced balance yields the Nusselt solution, which is associated with the following radial variation of the film height:

$$\delta^* = r^{*2/3}. \quad (145)$$

3.2 Pigford model

The Pigford model originally proposed by Wood & Watts (1973) represents an alternative approach to the TFE concept. The Pigford model solves the following set of equations for the depth-averaged velocities and the film height, written here in dimensional form:

$$r\bar{u}\delta = \frac{Q}{2\pi} \quad (146)$$

$$\bar{u}\frac{\partial\bar{u}}{\partial r} - \frac{\bar{v}^2}{r} = -\frac{12\pi^2 r^2 K_1 \nu_l}{Q^2}\bar{u}^3 \quad (147)$$

$$\bar{u}\frac{\partial\bar{v}}{\partial r} + \frac{\bar{u}\bar{v}}{r} = \frac{12\pi^2 r^2 K_2 \nu_l}{Q^2}\bar{u}^2(r\Omega - \bar{v}). \quad (148)$$

The essential difference to the TFE approach lies in the formulation of the

viscous term, which is determined in TFE based on the assumed velocity profile functions, while it is modeled in the Pigford approach using the expressions occurring on the rhs of Eqs. (147) and (148). It is noted that setting the model parameters $K_1 = K_2 = 1$ produces the Nusselt solution in the limit of large radii, where $\bar{v} = 0$, as well. The integration of the momentum equations (Eqs. (147) and (148)) uses the same radially inner boundary conditions at $r = r_i$, as the TFE solutions described by Eqs. (142)-(144).

4 Results

This section discusses in detail the results of the CFD simulation for the considered cases which were defined to cover a relevant range of operating condition in the real device. A comparison of the CFD results against approximate solutions is carried out as well.

4.1 Considered test cases

In total, eighteen test cases were specified varying the following three parameters: the nozzle-to-disk distance h_{nd} , the rotational speed of the disk n , and the volumetric flow rate Q of the dispensed liquid. The cases are listed in Table 4. The first half of them is associated with laminar, the second with turbulent inflow conditions. Water at $20^\circ C$ is assumed as working liquid, air at $20^\circ C$ is assumed as gaseous ambient medium. Constant densities and kinematic viscosities are used for both phases, $\rho_l = 998.2 \text{ kg/m}^3$, $\rho_g = 1.225 \text{ kg/m}^3$, $\nu_l = 10^{-6} \text{ m}^2/\text{s}$ and $\nu_g = 14.6 \times 10^{-6} \text{ m}^2/\text{s}$, respectively.

As already discussed in section 2.4.4, a uniform inflow velocity was always prescribed at the liquid inlet, so its value is simply determined by the considered volumetric flow rate and the nozzle diameter

$$v_{nozzle} = \frac{4Q}{d_{nozzle}^2 \pi}. \quad (149)$$

The diameter of the nozzle is $d_{nozzle} = 4 \text{ mm}$ for the case with laminar inflow ($Q = 0.3 \text{ lpm}$), and $d_{nozzle} = 4.82 \text{ mm}$ for the cases with turbulent inflow ($Q = 1.5 \text{ lpm}$). The corresponding Reynolds numbers, determined at the nozzle exit conditions as

$$Re = \frac{4Q}{d_{nozzle} \pi \nu_l}, \quad (150)$$

is $Re = 1\,532$ for the laminar cases (subcritical cases, since $Re < Re_{crit} = 2\,300$), and $Re = 6\,604$ for the turbulent cases (supercritical cases, since $Re > Re_{crit}$). The present specification of test cases was essentially guided by the intention to cover a representative range of operating conditions typically found in

	Case	rotational speed n [rpm]	nozzle-to-disk distance h_{nd} [mm]
Laminar inflow $Q = 0.3 \text{ lpm}$ (subcritical)	1a	60	17.5
	1b	60	35
	1c	60	70
	2a	500	17.5
	2b	500	35
	2c	500	70
	3a	1000	17.5
	3b	1000	35
	3c	1000	70
Turbulent inflow $Q = 1.5 \text{ lpm}$ (supercritical)	4a	500	17.5
	4b	500	35
	4c	500	70
	5a	1000	17.5
	5b	1000	35
	5c	1000	70
	6a	1500	17.5
	6b	1500	35
	6c	1500	70

Table 4: Test cases

the real process at Lam Research. Accordingly, the particular values for the volumetric flow Q were chosen to investigate practically relevant laminar and turbulent inflow conditions. The rotational speed n and the nozzle-to-disk distance h_{nd} were varied within a feasible range for the existing device. The standard nozzle-to-disk distance, which is presently used in the existing machines, is 35 mm .

4.2 Numerical results

4.2.1 Centerline velocity of the impinging liquid jet

Since the rotational speed of the disk has shown no influence on the solutions for the centerline velocity v_c in the vertical liquid jet, the results for this quantity are discussed only for the case $n = 500 \text{ rpm}$. Figures 16 and 17

depict the variation of the axial centerline velocity with the distance from the impingement point for the different nozzle-to-disk distances. Starting from the nozzle exit velocity, being $v_{nozzle} = 0.4 \text{ m/s}$ for the laminar cases with $Q = 0.3 \text{ lpm}$, and $v_{nozzle} = 1.37 \text{ m/s}$ for the turbulent cases with $Q = 1.5 \text{ lpm}$, the centerline velocity increases with decreasing distance to the wall (located at $z = 0$) due to the gravitational forces. The curves essentially follow the solution obtained from the Bernoulli equations as

$$v_B(z) = \sqrt{v_{nozzle}^2 + 2g(h_{nd} - z)}, \quad (151)$$

which is shown as dashed lines in Figures 16 and 17 as well. When the impinging liquid approaches the point of stagnation at $z = 0$, the centerline velocity is rapidly decreased to zero as expected. In the laminar cases with $Q = 0.3 \text{ lpm}$ growing oscillations are observed as the flow gets closer to the impingement point at $z = 0$, most notably for the nozzle-to-disk distance $h_{nd} = 70 \text{ mm}$. These oscillations can be explained by the formation of capillary waves on the liquid-gas interface as seen from Figure 18 by the instantaneous radial positions of the interface. The depicted contour lines basically show an instantaneous snapshot of the shape of the liquid surface. Capillary waves typically occur in liquid columns moving through a quiescent gaseous medium at relatively low velocity. The long wave components of these perturbations tend to grow downstream, and would finally lead to the so called capillary breakup of the liquid column into individual droplets. The formation and growth of these capillary waves is demonstrated in Figure 18 by the black contour line, which represents the numerical results for a liquid jet issuing with the same nozzle exit conditions into an open domain without impingement on a rotating disk further downstream. The oscillations show approximately the same wave lengths, but the amplitudes are evidently increased due to the impingement on the disk as compared to the open domain case with no disk. The formation of large capillary waves upstream of the impingement is not observed in the cases with turbulent inflow ($Q = 1.5 \text{ lpm}$) as seen from Figure 19. This observation is consistent with the classical theory on the disintegration of liquid jets proposed by von Ohnesorge, which

distinguishes individual regimes of break-up dependent of the Reynolds and the Ohnesorge numbers. Computing for the different considered cases the Reynolds and the Ohnesorge numbers based on the local conditions at the impingement

$$Re = \frac{v_{imp}d_{imp}}{\nu_l}, \quad Oh = \frac{\nu_l\rho_l}{\sqrt{\sigma\rho_l d_{imp}}} \quad (152)$$

with the impact velocity v_{imp} obtained from Eq. (151) for $z = 0$ as

$$v_{imp} = \sqrt{v_{nozzle}^2 + 2gh_{nd}}, \quad (153)$$

and the diameter

$$d_{imp} = \sqrt{\frac{4Q}{\pi v_{imp}}}, \quad (154)$$

introducing the obtained Re - Oh -pairs into the regime diagram shown in Figure 20 demonstrates that the laminar cases lie well within the regime of the capillary breakup. In contrast, the turbulent cases lie already in the wind-induced regime, where typically disturbances of small wave length are generated by aerodynamical forces of the ambient gas acting on the liquid surface. Some small scale oscillations are visible for the largest nozzle-to-disk distance in turbulent cases (Figure 19), but they practically never reach a significant level to influence the conditions further downstream.

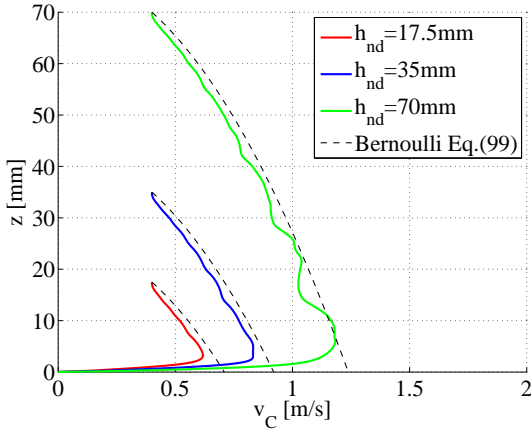


Figure 16: Centerline velocity vs. distance from the disk for varying nozzle-to-disk distances h_{nd} , $Q = 0.3 \text{ lpm}$, $n = 500 \text{ rpm}$

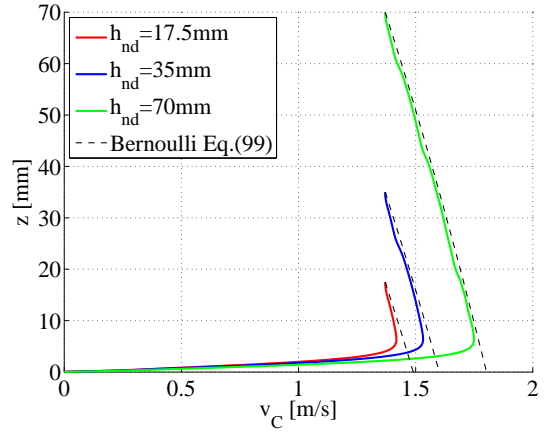


Figure 17: Centerline velocity vs. distance from the disk for varying nozzle-to-disk distances h_{nd} , $Q = 1.5 \text{ lpm}$, $n = 500 \text{ rpm}$

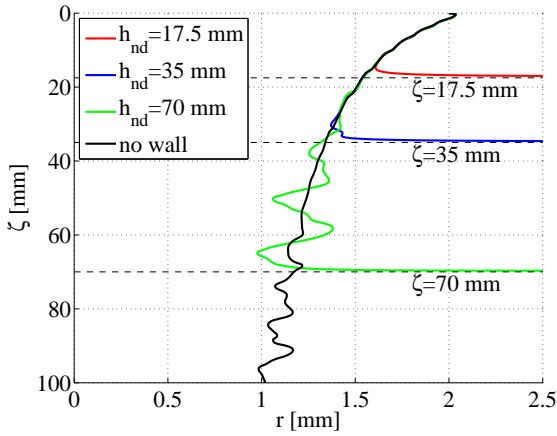


Figure 18: Instantaneous radial position of the interface r_δ vs. distance from the nozzle $\zeta = h_{nd} - z$, $Q = 0.3 \text{ lpm}$, $n = 500 \text{ rpm}$

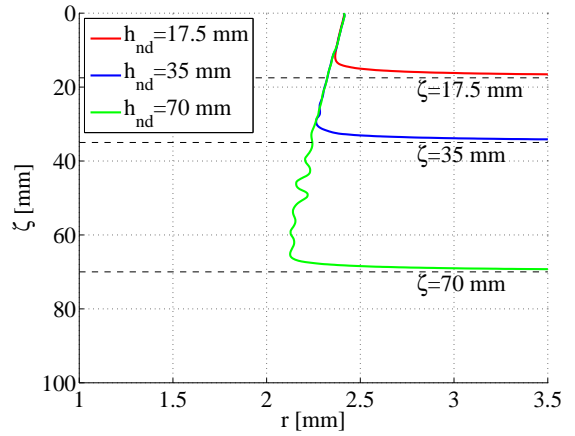


Figure 19: Instantaneous radial position of the interface r_δ vs. distance from the nozzle $\zeta = h_{nd} - z$, $Q = 1.5 \text{ lpm}$, $n = 500 \text{ rpm}$

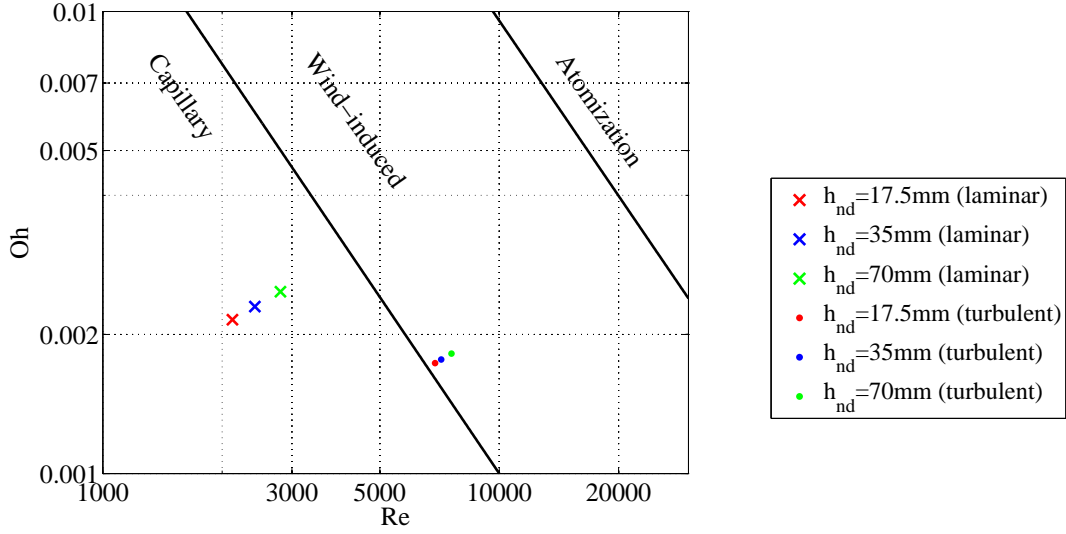


Figure 20: Regimes of liquid jet breakup (von Ohnesorge (1936))

4.2.2 Film thickness and mean radial velocity

Figures 21-26 and 27-32 show the time averaged radial profiles of the film thickness δ and the radial mean velocity \bar{u} of the liquid, which were obtained for the laminar and turbulent inflow conditions, associated with $Q = 0.3 \text{ lpm}$ and $Q = 1.5 \text{ lpm}$, respectively, varying the nozzle-to-disk distance and the rotational speed. The radial mean velocity of the liquid film is defined as

$$\bar{u} = \frac{1}{\delta} \int_0^{\delta} \alpha u dz. \quad (155)$$

As such it basically represents the depth-averaged value of the liquid velocity obtained from the VOF-based simulations. It is noted that the strong oscillations exhibited in radially outer region for the solutions with the higher rotational speeds due to the computational restrictions on the time span, over which the presented statistics was sampled. Owing to the comparatively strong temporal fluctuations in the instantaneous solutions for the higher rotational speeds this time span would have needed to be markedly increased

to obtain smoother averaged results throughout the domain. This, however, would have lead to unacceptably long computational run times for each case. More importantly, the observed oscillations do not affect the focused region of interest (central region around the impingement), so that they have practically no relevance for the essential findings and conclusions obtained from the results. A significant influence of the nozzle-to-disk distance appears only in the region near the center of the disk. The higher vertical momentum of the impinging liquid for the higher nozzle-to-disk distances translates evidently into a higher momentum into the horizontal radial direction after the impingement. This finally leads to higher radial mean velocities and, in effect, a smaller film thickness for the higher nozzle-to-disk distances in the central region. This behavior persists, as long as the inertia, i.e. the initial momentum, of the impinging liquid plays a dominant role. Very next to the impingement point ($r = 0$) the mean radial velocities reach peak values, which are only about 12-15% smaller than the impact velocity v_{imp} obtained from the Bernoulli equation (Eq. (153)), which represents an ideal reference velocity free of any losses. For all considered nozzle-to-disk distances, most part of the oncoming vertical momentum is evidently redirected into horizontal (radial) momentum with relatively small fluid dynamic losses. As the radial distance from the center increases, the flow becomes dominated by centrifugal and viscous forces, while the inertial forces become insignificant. The vanishing effect of the initial momentum (=inertial forces) is clearly indicated by the convergence of the radial profiles of the film thickness and the averaged radial velocity obtained for the different values of h_{nd} . A comparison of the results for the different rotational speeds makes further evident that the radial extension of the central region, where the inertia, and hence the nozzle-to-disk distance are of relevance, decreases with increasing rotational speed. Accordingly, the region, where the radial profiles essentially collapse into one curve moves towards the center for the higher rotational speeds. This observation is also well in line with the fact that region of agreement with the analytical (Nusselt) solution, which is computed from a balance of the viscous and the centrifugal forces neglecting inertia, is extended radially inwards for the higher rotational speeds.

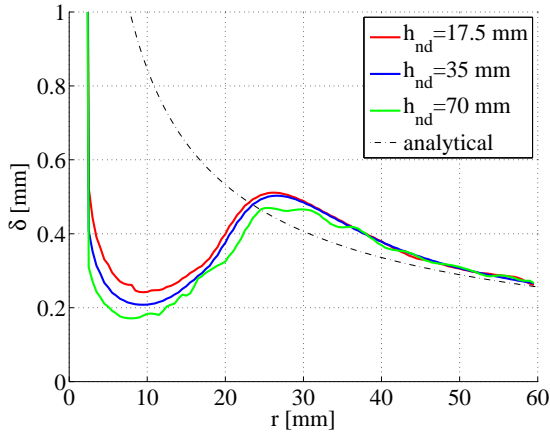


Figure 21: Time averaged film thickness, $n = 60 \text{ rpm}$, $Q = 0.3 \text{ lpm}$

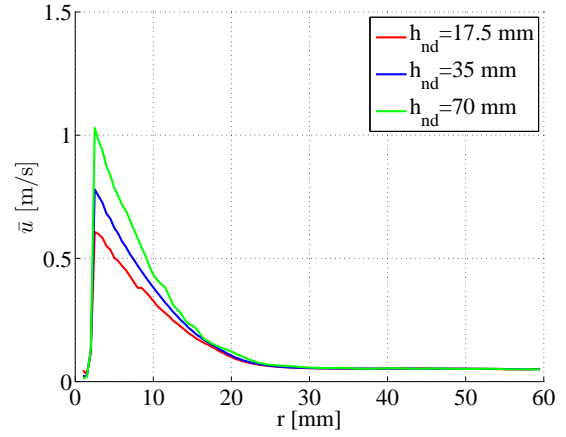


Figure 24: Time averaged radial mean velocity, $n = 60 \text{ rpm}$, $Q = 0.3 \text{ lpm}$

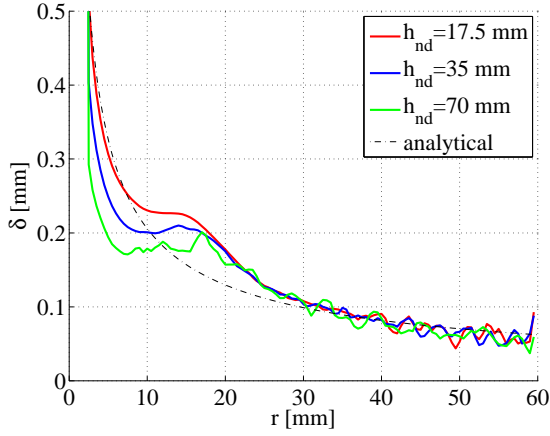


Figure 22: Time averaged film thickness, $n = 500 \text{ rpm}$, $Q = 0.3 \text{ lpm}$

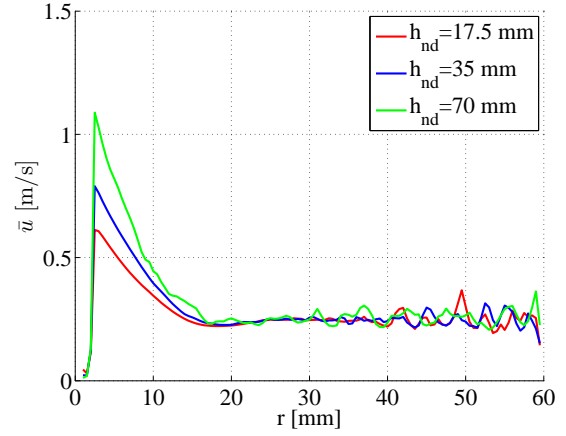


Figure 25: Time averaged radial mean velocity, $n = 500 \text{ rpm}$, $Q = 0.3 \text{ lpm}$

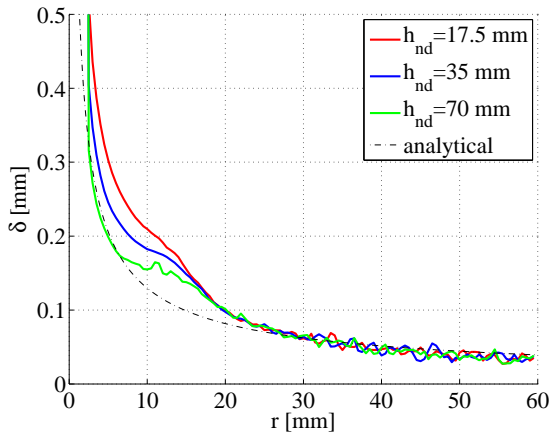


Figure 23: Time averaged film thickness, $n = 1000 \text{ rpm}$, $Q = 0.3 \text{ lpm}$

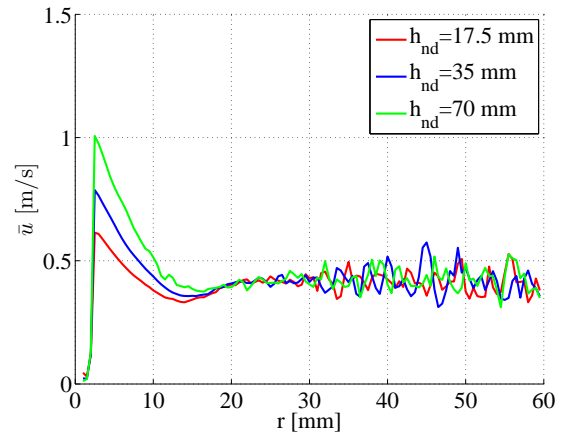


Figure 26: Time averaged radial mean velocity, $n = 1000 \text{ rpm}$, $Q = 0.3 \text{ lpm}$

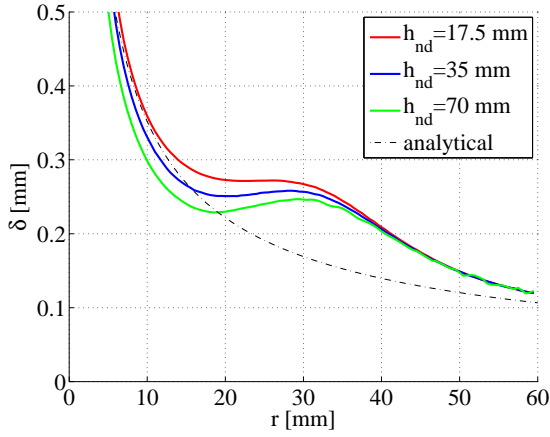


Figure 27: Time averaged film thickness, $n = 500 \text{ rpm}$, $Q = 1.5 \text{ lpm}$

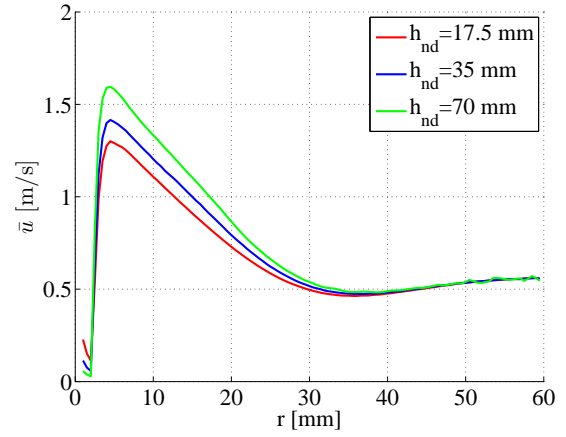


Figure 30: Time averaged radial mean velocity, $n = 500 \text{ rpm}$, $Q = 1.5 \text{ lpm}$

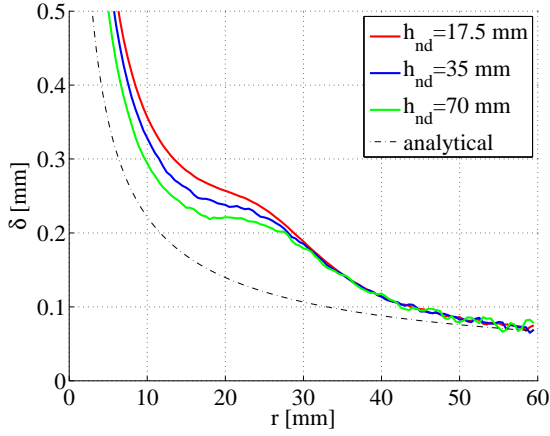


Figure 28: Time averaged film thickness, $n = 1000 \text{ rpm}$, $Q = 1.5 \text{ lpm}$

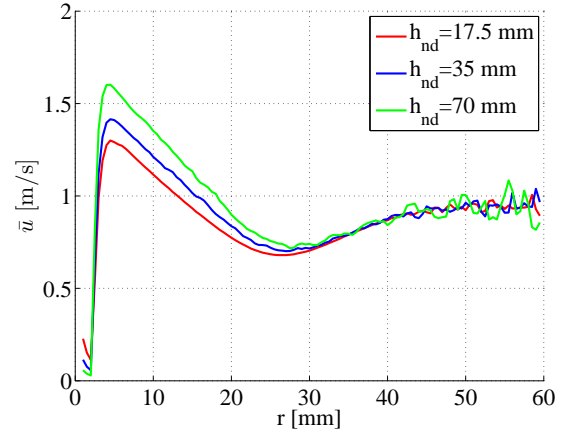


Figure 31: Time averaged radial mean velocity, $n = 1000 \text{ rpm}$, $Q = 1.5 \text{ lpm}$

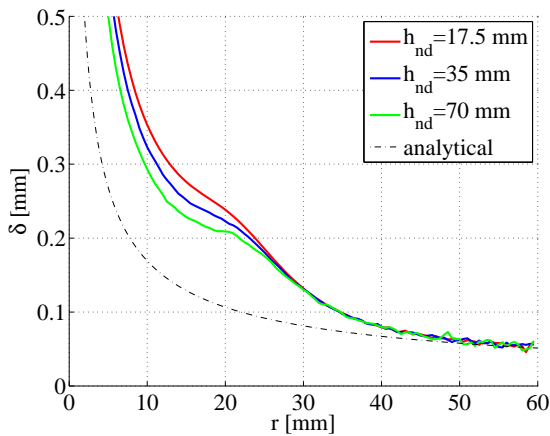


Figure 29: Time averaged film thickness, $n = 1500 \text{ rpm}$, $Q = 1.5 \text{ lpm}$

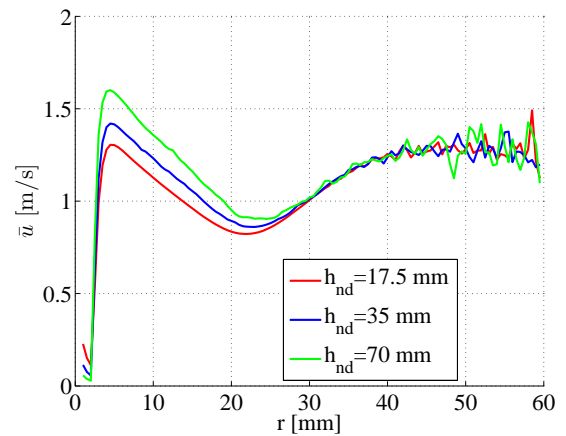


Figure 32: Time averaged radial mean velocity, $n = 1500 \text{ rpm}$, $Q = 1.5 \text{ lpm}$

4.2.3 Wall shear stress

The time averaged radial variations of the wall shear stress obtained for the laminar and turbulent inflow conditions are shown in Figures 33-35 and 36-38, respectively.

The wall shear stress defined as

$$\tau_w = \rho_l \nu_l \left. \frac{\partial u}{\partial z} \right|_{z=0} \quad (156)$$

basically measures the gradient of the radial velocity at the wall. Due to the analogy between momentum transfer and mass transfer, the wall shear stress can also be used to identify regions of intense diffusive mass transfer, which is associated with high local etching rates in the limit of fast, diffusion-controlled, chemistry.

In the thin film flow regime the wall shear stress essentially follows the ratio of the mean radial liquid velocity to the film thickness

$$\tau_w \sim \frac{\bar{u}}{\delta}. \quad (157)$$

This dependence is also clearly seen in the present results. In the central region, which is dominated by inertia, the wall shear stress is highest for the highest nozzle-to-disk distance, where the highest mean radial velocities \bar{u} lead to the smallest film heights δ . In the turbulent cases (Figures 36-38) the individual solutions notably diverge in the region between $r = 10 \text{ mm}$ and $r = 30 \text{ mm}$. This particular feature, which does not occur in the laminar cases (Figure 33-35), is observed most pronouncedly for the high h_{nd} values with the lowest rotational speed (Figure 36), and it can be attributed to a local influence of turbulence. It is supposed that turbulence increases here the effective viscosity resulting in a higher wall friction, and hence a higher value of τ_w . The effect of turbulence will be discussed in more detail in section 4.2.5.

It is also interesting to see that the maxima of the wall shear stress in the impingement region, which are due to the rapid redirection of the oncoming liquid from vertical into the horizontal motion leading to high local near wall

velocity gradients are markedly exceeded by the shear stress levels in the radially outer region for the highest rotational speed (Figure 38). The higher the rotational speed, the smaller is evidently the overall effect of the initial momentum of the vertically impinging liquid, and hence the effect of the nozzle-to-disk distance. This is again clearly indicated by the convergence of the individual solutions to a single curve in all cases.

Recalling the radial length scale defined in Eq. (96) as originally proposed by Rauscher *et al.* (1973) with Eq. (165) where $\Omega = 2n\pi/60$ denotes the angular speed, the radial extension of the region, which is influenced by the nozzle-to-disk distances, can be estimated as

$$r_{infl} = C l_0. \quad (158)$$

The value of the parameter C can be determined by defining r_{infl} as the radial distance, beyond which the solutions obtained for varying h_{nd} practically collapse into one single curve. The so obtained values for C together with the corresponding values of r_{infl} are listed for the different cases in Table 5. The very small variation of the parameter C indicates that the proposed correlation (Eq. (158)) with $C \approx 0.92$ provides a very reliable estimate for the size of the central region, which is influenced by the nozzle-to-disk distance.

Subcritical inflow $Q = 0.3 \text{ lpm}$			Turbulent inflow $Q = 1.5 \text{ lpm}$		
n [rpm]	r_{infl} [mm]	C	n [rpm]	r_{infl} [mm]	C
60	28	0.9073	500	37	0.9110
500	17	0.9359	1000	31	0.9077
1000	14	0.9166	1500	28	0.9073

Table 5: Parameter C and r_{infl} for the considered variation of flow rates and rotational speeds

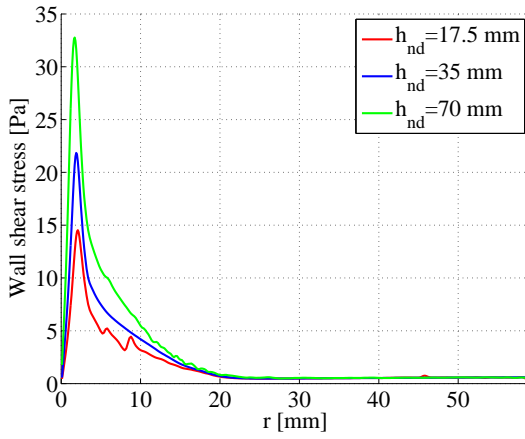


Figure 33: Time averaged wall shear stress, $n = 60 \text{ rpm}$, $Q = 0.3 \text{ lpm}$

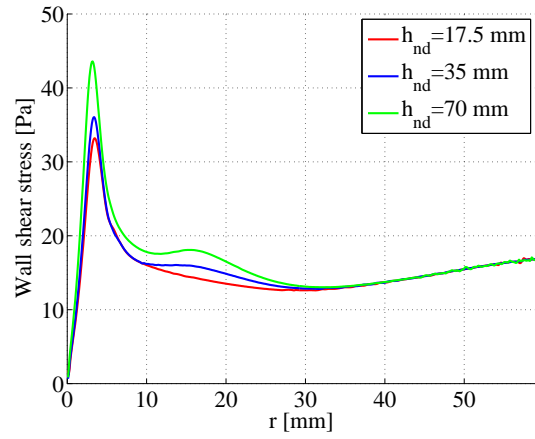


Figure 36: Time averaged wall shear stress, $n = 500 \text{ rpm}$, $Q = 1.5 \text{ lpm}$

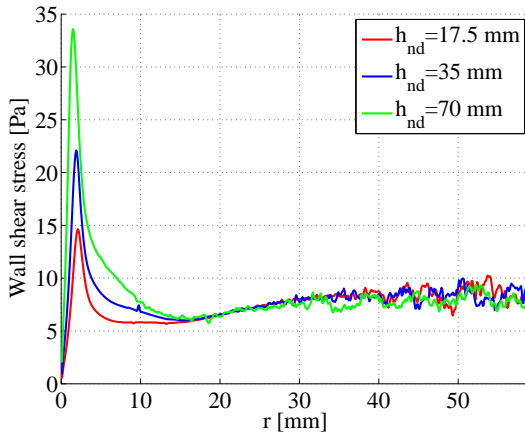


Figure 34: Time averaged wall shear stress, $n = 500 \text{ rpm}$, $Q = 0.3 \text{ lpm}$

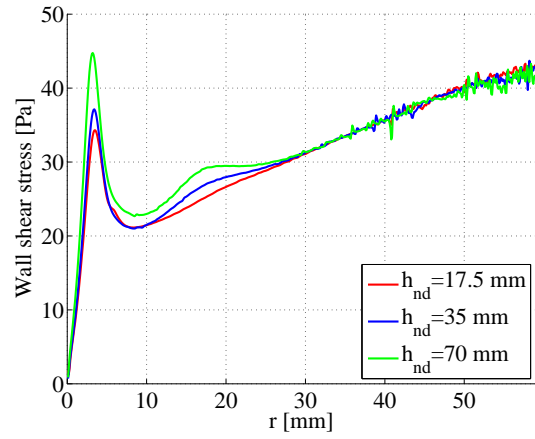


Figure 37: Time averaged wall shear stress, $n = 1000 \text{ rpm}$, $Q = 1.5 \text{ lpm}$

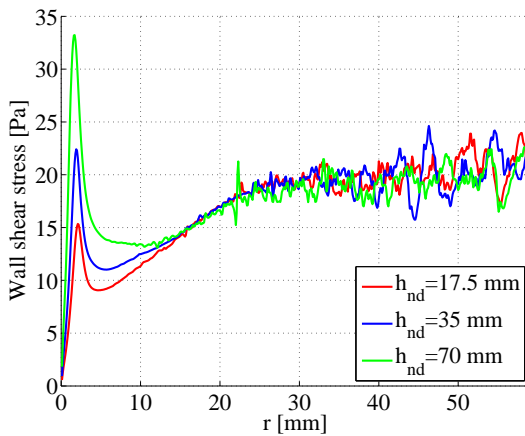


Figure 35: Time averaged wall shear stress, $n = 1000 \text{ rpm}$, $Q = 0.3 \text{ lpm}$

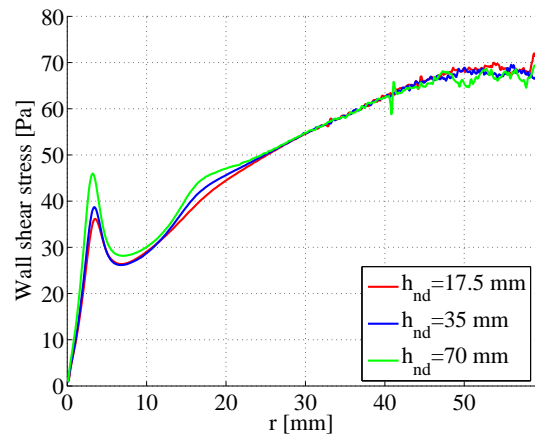


Figure 38: Time averaged wall shear stress, $n = 1500 \text{ rpm}$, $Q = 1.5 \text{ lpm}$

4.2.4 Local velocity profiles inside the liquid film

The local profiles of the radial velocity component obtained at different radial positions are shown in Figure 39 for laminar, and in Figure 40 for turbulent inflow. The solid lines refer to the liquid phase, and the dotted lines refer to the gaseous phase of the ambient air above the film. The growing waviness of the film, which was observed especially for the low flow rate (laminar inflow) at higher rotational speeds, also translates into strong temporal variations of the local velocity. Therefore, all local profiles shown for the laminar inflow ($Q = 0.3 \text{ lpm}$) are averaged in time to allow for a meaningful comparison of the different cases. The shown profiles essentially confirm in more detail the findings obtained from the variations of the radial mean velocity along the disk displayed in the Figures 24-26 and 30-32 above. In the central region, which can be identified here as region within $0 < r < r_{infl}$ with values for r_{infl} listed in Table 5, the local radial velocities are always higher for the higher nozzle-to-disk distances pointing again at the dominance of the inertial forces associated with the oncoming initial momentum. The for continuity reason thinner film thickness for the higher velocities also leads to steeper velocity gradients resulting in higher wall shear stresses according to Eq. (156) for the higher nozzle-to disk distances. The central region further appears to be unaffected by the centrifugal forces, as seen from a comparison of the profiles for the different rotational speeds. In the radially outer region, associated with $r > r_{infl}$, the velocity profiles practically collapse, showing again the vanishing effect of the initial momentum of the impinging liquid in this outer zone. On the other hand, the strong influence of the centrifugal forces associated with the different rotational speeds becomes well visible in the profiles obtained for $r > r_{infl}$. For the higher rotational speeds the higher centrifugal forces evidently accelerate the flow to higher radial velocities. Concerning the vanishing influence of the initial momentum of the impinging liquid in the radially outer region, the laminar and the turbulent cases show basically the same behavior. In the central region, the turbulent cases (computed with the SST $k-\omega$ model) generally exhibit bulkier profiles as compared to the laminar cases. Since in the laminar case associated with markedly smaller volumetric

flow rates the film surface tends to exhibit considerable unsteady waviness in the outer radial region, the velocity profiles are averaged in time. In contrast, the surface of turbulent cases, where the flow rate is much higher, remained generally smooth, so that averaging of the profiles was not necessary.

4.2.5 Effect of turbulence

The higher considered flow rate $Q = 1.5 \text{ lpm}$ implies turbulent inflow conditions, because the corresponding nozzle exit Reynolds number defined in Eq. (150) exceeds the critical limit $Re_{crit} = 2300$. As a consequence, the liquid flow has to be assumed as turbulent, at least in the central region around the impingement. The $k\text{-}\omega\text{-SST}$ model was used in the present simulation as default turbulence model. In one selected case the realizable $k\text{-}\epsilon$ model was used as an alternative model. Based on the superposition given in Eq. (25) the turbulent viscosity ratio defined as

$$\beta = \frac{\nu_t}{\nu_l}. \quad (159)$$

provides an appropriate measure for the dynamic effect of the turbulence on the motion of the fluid. Figures 41-43 show the radial variation of this quantity along the disk, using in Eq. (159) a mean turbulent viscosity $\bar{\nu}_t$, which has been averaged over the film height analogously to Eq. (155) rewritten as

$$\bar{\nu}_t = \frac{1}{\delta} \int_0^\delta \alpha \nu_t dz, \quad (160)$$

and averaged in time as well.

It becomes evident that the effect of turbulence is present only in the central region, while the flow is laminar in the outer region, where the viscosity ratio drops to zero. We see again a convergence of the solutions for the different nozzle-to-disk distances h_{nd} for increasing radii r . In the central region, the smaller nozzle-to-disk distances exhibit higher levels of β . This particular feature can be explained by the level of the oncoming turbulence ahead of the impingement. Figure 44 shows the streamwise variation of the turbulent

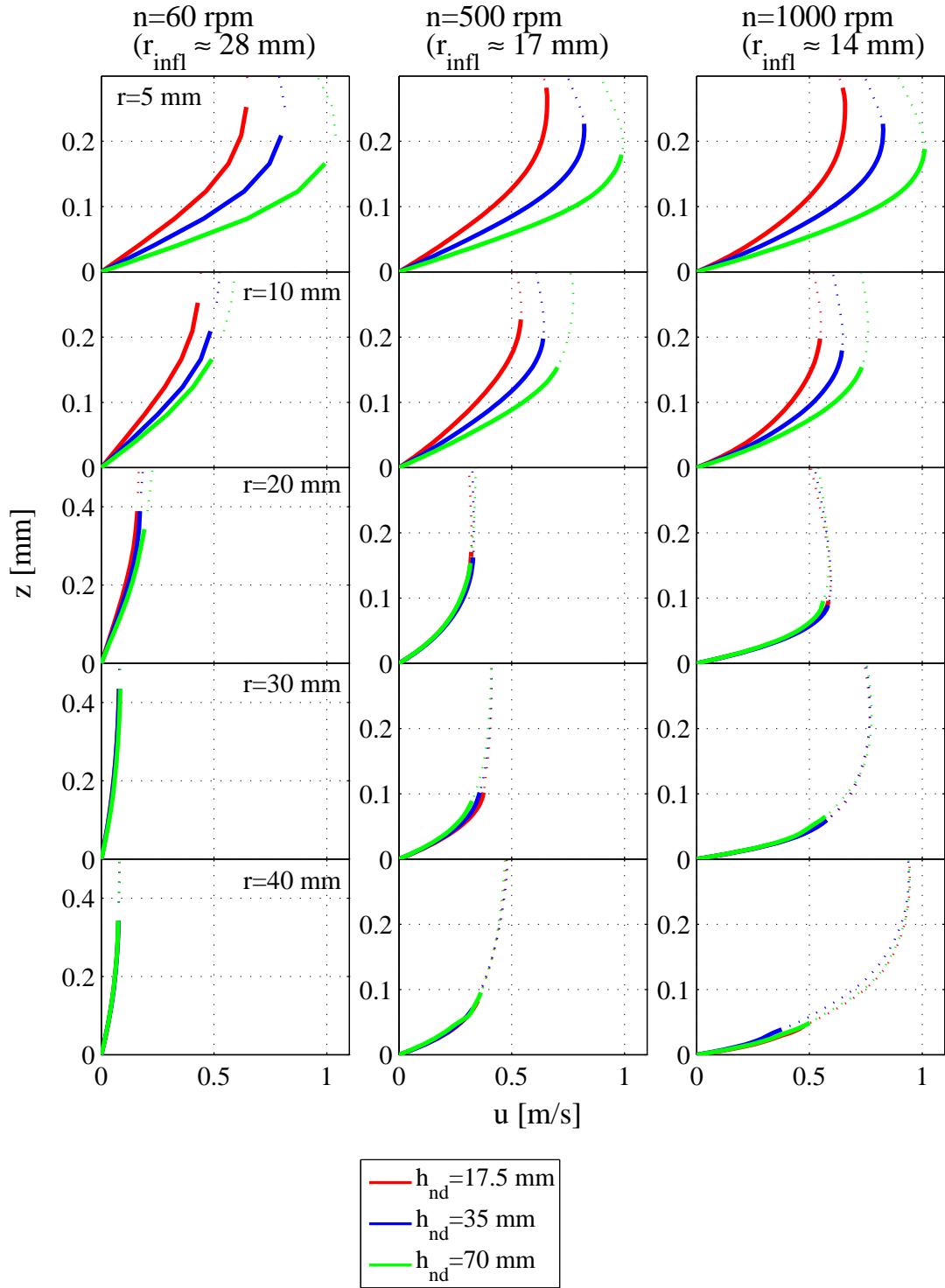


Figure 39: Time Averaged radial velocity profiles at $r = 5/10/20/30/40$ mm for three different rotational speeds, $Q = 0.3$ lpm

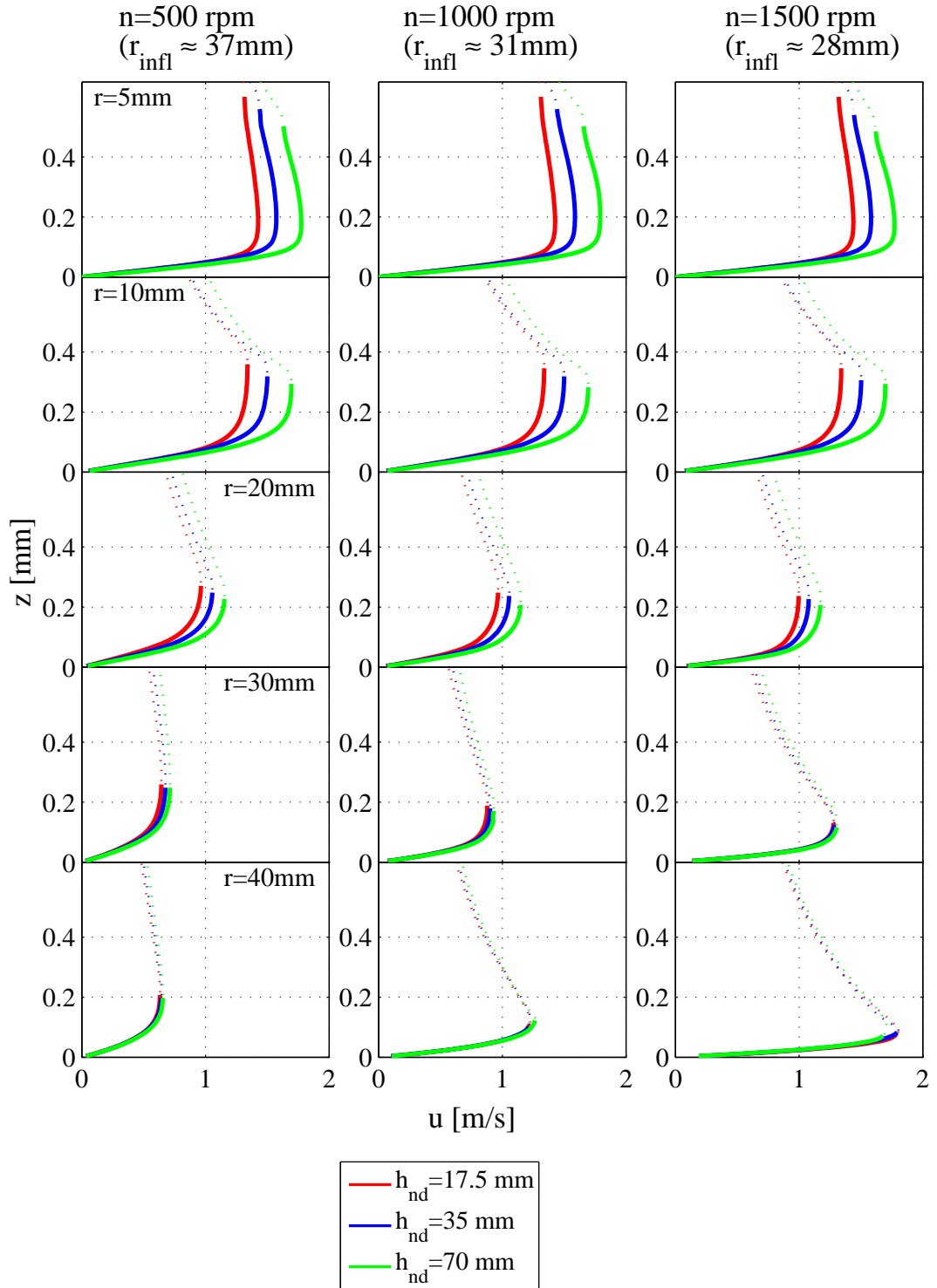


Figure 40: Instantaneous radial velocity profiles at $r = 5/10/20/30/40$ mm for three different rotational speeds, $Q = 1.5$ lpm

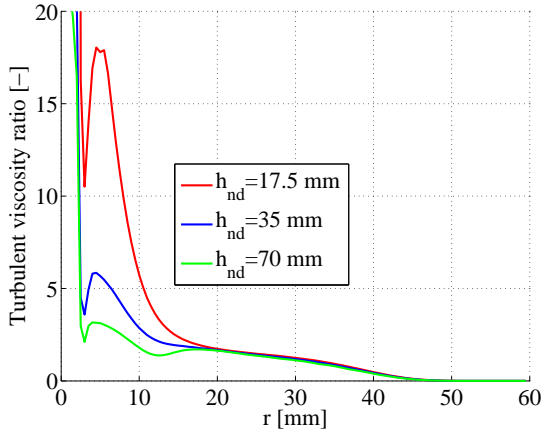


Figure 41: Time averaged mean turbulent viscosity ratio $\beta = \overline{\nu_t}/\nu_l$, $n = 500$ rpm, $Q = 1.5$ lpm

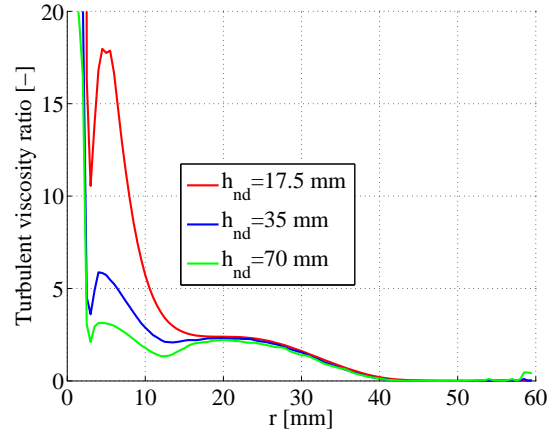


Figure 42: Time averaged mean turbulent viscosity ratio $\beta = \overline{\nu_t}/\nu_l$, $n = 1000$ rpm, $Q = 1.5$ lpm

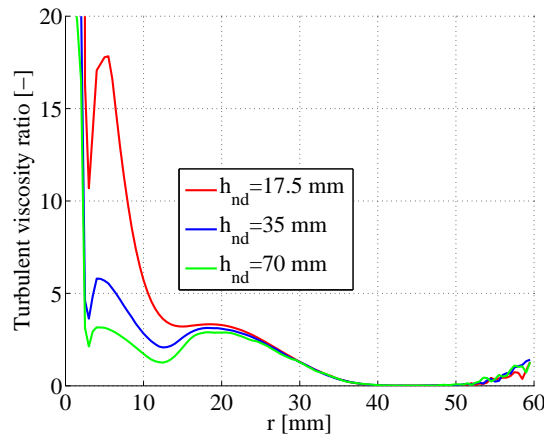


Figure 43: Time averaged mean turbulent viscosity ratio $\beta = \overline{\nu_t}/\nu_l$, $n = 1500$ rpm, $Q = 1.5$ lpm

kinetic energy between the nozzle and the disk. Being defined as the kinetic energy contained in the turbulent fluctuating velocity components

$$k = \frac{\overline{u'^2} + \overline{v'^2} + \overline{w'^2}}{2}, \quad (161)$$

this quantity basically measures the intensity of the turbulent motion. As such it is strongly related to the eddy viscosity, $\nu_t \sim k$. The solid lines refer to the variation of k exactly along the center line of the jet, the dashed lines refer to the streamwise variation inside the liquid along an off-center line at a radial distance $r = 2\text{ mm}$. The turbulence which is introduced at the inlet considerably decreases downstream of the nozzle. The strain-based production of turbulent kinetic energy is here evidently too small to balance the losses due to viscous dissipation and the gravity-driven streamwise acceleration. However, very next to the impingement, as shown by the zoom into the near-disk region in figure 45, the rate of strain is significantly increased due to the strong linear deformation of the oncoming liquid, so that the strongly enhanced production of turbulence leads to peak values of the turbulent kinetic energy near $z = 0$.

In summary, it can be stated that the smaller the nozzle-to-disk distance, the larger portion of the nozzle inlet turbulence is preserved until impingement. The resulting higher level of turbulent kinetic energy in the impingement region lets also expect a more intense etching activity for lower values of h_{nd} . In order to analyze in more detail to which extent the turbulence changes the essential film flow quantities like film thickness, wall shear stress, or, the velocity profiles inside the film, the case 4b with $Q = 1.5\text{ lpm}$ and $h_{nd} = 35\text{ mm}$ was also simulated assuming laminar flow, i.e., without turbulence model. Additionally, this case was simulated using the k - ϵ Realizable model as an alternative turbulence model to get some insight into the sensitivity of the solution to the chosen turbulence model.

The results of these additional simulations are shown in Figures 46-48 plotted together with the corresponding results obtained with the k - ω -SST turbulence model. The two alternative turbulence models give evidently very

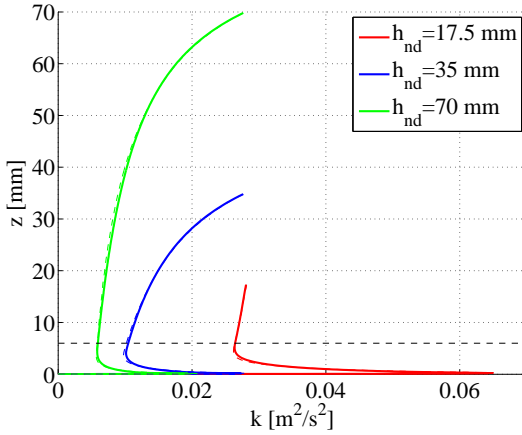


Figure 44: Turbulent kinetic energy along the centerline (solid line) and a parallel off-center line at radial distance $r = 2 \text{ mm}$ (dashed line) for varying nozzle-to-disk distances h_{nd} , $Q = 1.5 \text{ lpm}$, $n = 500 \text{ rpm}$

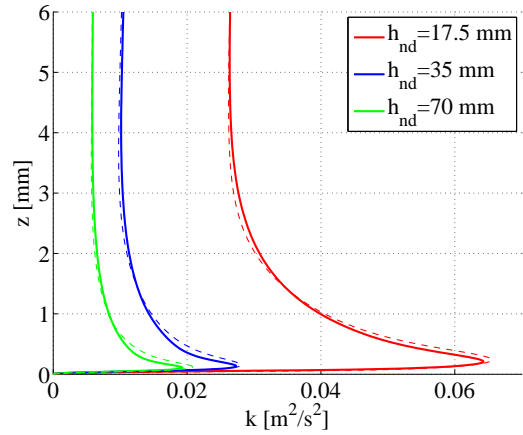


Figure 45: Zoom into near disk region shown in Figure 44

similar results. In contrast, the laminar solution exhibits a notably smaller film thickness in the middle of the domain, which is consistent with the lower wall shear stress seen in Figure 47. The comparatively lower wall shear stress is also indicated by the velocity profiles for the inner region ($r \approx 15 \text{ mm}$) in Figure 48, where both turbulent solutions exhibit more bulky profiles associated with steeper wall gradients. The $k-\omega$ SST model predicts somewhat higher velocity gradients at the wall in this region as compared to the $k-\epsilon$ Realizable model. This is also clearly seen in Figure 47, where the $k-\omega$ SST model exhibits the highest wall shear stress in the zone around $r = 15 \text{ mm}$. In summary, it can be concluded that the turbulence tends to increase the wall shear stress as it produces additional frictional losses. The streamwise motion becomes effectively more retarded leading to thicker liquid films for continuity reason.

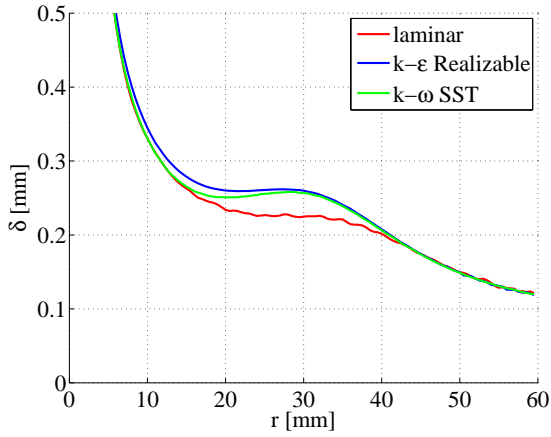


Figure 46: Time averaged film thickness, $n = 500 \text{ rpm}$, $Q = 1.5 \text{ lpm}$, $h_{nd} = 35 \text{ mm}$

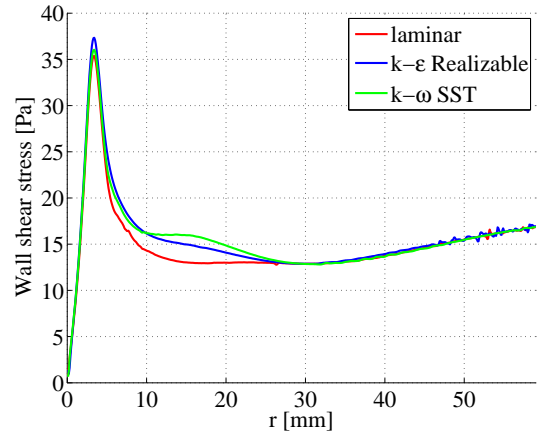


Figure 47: Time averaged wall shear stress, $n = 500 \text{ rpm}$, $Q = 1.5 \text{ lpm}$, $h_{nd} = 35 \text{ mm}$

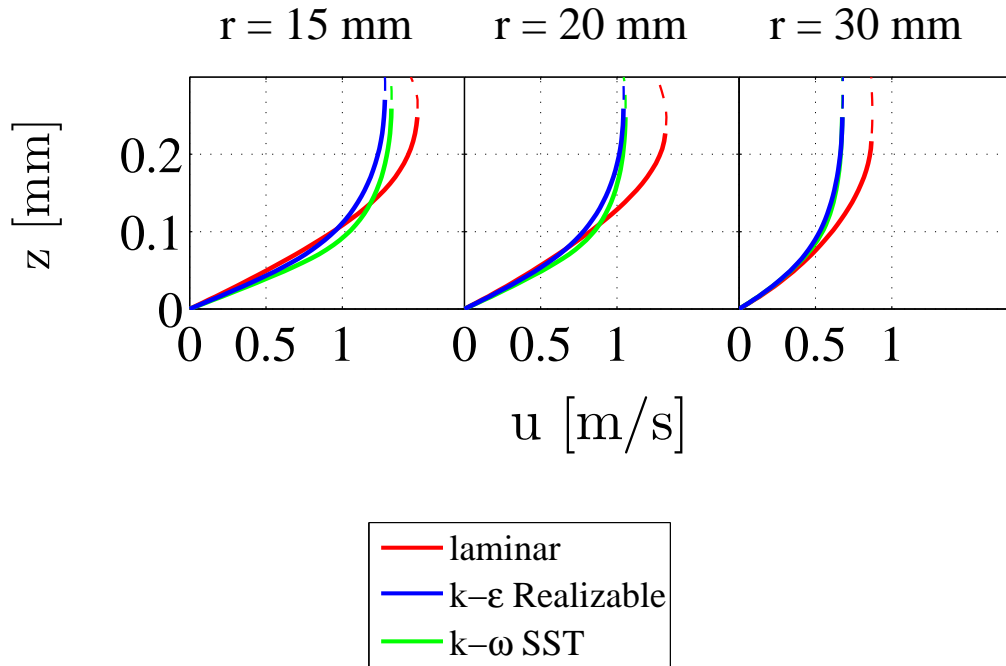


Figure 48: Instantaneous radial velocity profiles at selected radial positions for $n = 500 \text{ rpm}$, $Q = 1.5 \text{ lpm}$, $h_{nd} = 35 \text{ mm}$

Figure 49 shows the radial variations of the vertical distance of first near-wall node (located at $z = z_{WP}$) to the wall in terms of the corresponding wall coordinates

$$z_W^+ = \frac{u_\tau z_{WP}}{\nu}. \quad (162)$$

The wall coordinates of the surface of the film

$$z_\delta^+ = \frac{u_\tau \delta}{\nu} \quad (163)$$

are shown in Figure 50. The presentation in wall coordinates gives some insight into the structure of the boundary layer inside the liquid film. The fairly small z^+ -values at the film surface indicate that a large part of the liquid film, except the inner region near the impingement, belongs to the viscous sublayer ($z^+ < 5$) or to the buffer layer ($5 \leq z^+ \leq 30$), so that the near-wall modeling plays an important role in the results of both turbulence models. As seen from the variation of the wall-coordinate of the first near-wall point, the values of z_W^+ remain always well below $z^+ = 1$. This proves the near-wall resolution as sufficiently fine for the near-wall modeling applied in the simulations.

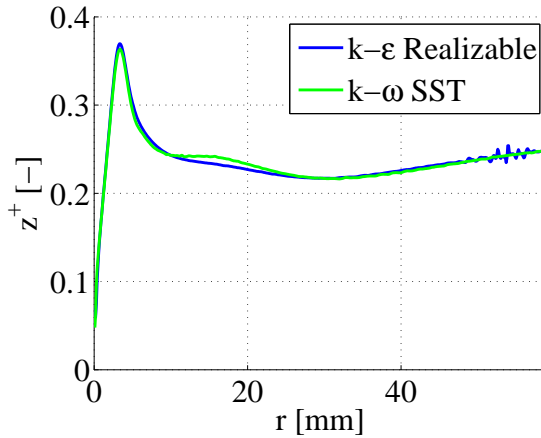


Figure 49: z^+ -values at the first near-wall node for the different turbulence models, $h_{nd} = 35 \text{ mm}$, $Q = 1.5 \text{ lpm}$, $n = 500 \text{ rpm}$

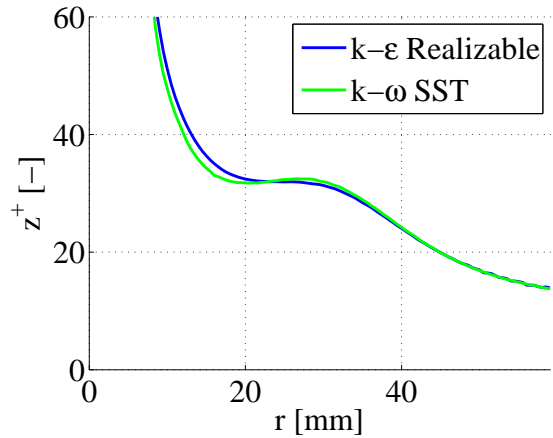


Figure 50: z^+ -values at the surface for the different turbulence models, $h_{nd} = 35 \text{ mm}$, $Q = 1.5 \text{ lpm}$, $n = 500 \text{ rpm}$

Figures 51-53 show the variations of the turbulent kinetic energy, the turbulent energy production, and the turbulent viscosity ratio along the centerline of the radial jet very close to the impingement point at $z = 0$, respectively. It becomes evident that the k - ϵ Realizable model predicts a markedly higher level of turbulent kinetic energy associated with a higher production near the impingement. This translates into a higher turbulent viscosity ratio, as seen from Figure 53.

4.3 Comparison against approximate solutions

In the following the results of the numerical simulation shall be compared against approximate solutions, which have been obtained from the simplified concepts using the Thin Film Equations (TFE) and the Pigford model. The formulation of both approaches was presented in section 3. Both Approximations have in common that they reduce the dimensionality of the film flow problem by solving a simplified set of the equations of motion for the depth-averaged velocity components \bar{u} , \bar{v} , generally defined by Eq. (115), and the film height δ . In the Pigford model the introduction of model parameters K_1 and K_2 , offers some more freedom to describe the effect of the viscous forces as compared to TFE. The two parameters are commonly set to values within the range 0.5 to 0.7. In the present case an equal setting is used for both parameters, so that $K_1 = K_2 = K$. Figures 55-60 show radial profiles of the film thickness obtained with the approximate formulations (Nusselt, Pigford, TFE) for varying the nozzle-to-disk distances compared against the corresponding time averaged results of the CFD simulation. The Nusselt solution represents the asymptotic TFE solution in the limit of large radii. For the TFE and Pigford the same inflow conditions are prescribed at the in radially inner boundary $r = r_i$. They are written as

$$r = r_i = d_{imp} \quad : \quad \bar{u} = v_{imp} \quad (164)$$

$$\delta_i = \frac{Q}{d_{imp}\pi v_{imp}} \quad (165)$$

with v_{imp} and d_{imp} obtained from Eqs. (153) and (154), respectively. Imposing an impact velocity v_{imp} dependent on h_{nd} , the inner boundary condition accounts for variation of the nozzle-to-disk distance h_{nd} . While the TFE and the Pigford model solution agree fairly well with the numerical CFD solution in the radially outer region, both approaches tend to underpredict the local minimum in the film thickness near the center. For the turbulent case associated with $Q = 1.5\text{ lpm}$ the prediction of the Pigford model can be improved using a higher value of the model parameter K , as demonstrated in Figures 58-60 by the solutions obtained with $K = 1$. Setting this parameter to a higher value effectively increases the viscous forces retarding the radial motion, which thickens the film especially in the central region. In the turbulent flow regime using an increased value for K appears to be plausible, as it reflects the increased effective viscosity due to the turbulent contribution shown in Eq. (25).

The Nusselt solution approaches all the other results only in the radially outer region (large radii) as expected.

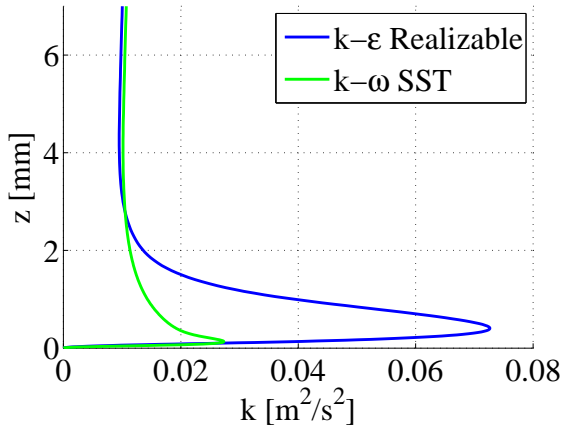


Figure 51: Turbulent kinetic energy along the centerline with two different turbulence models, $h_{nd} = 35 \text{ mm}$, $Q = 1.5 \text{ lpm}$, $n = 500 \text{ rpm}$

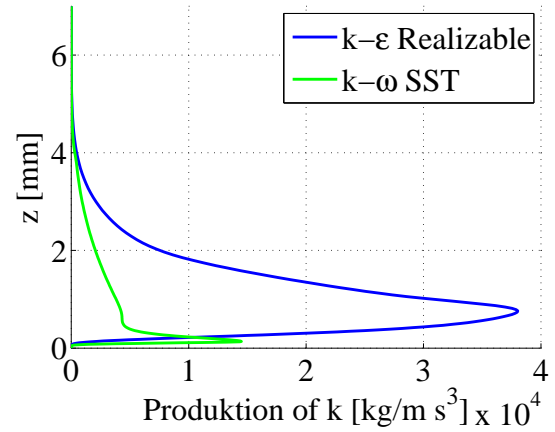


Figure 52: Produktion of the turbulent kinetic energy along the centerline with two different turbulence models, $h_{nd} = 35 \text{ mm}$, $Q = 1.5 \text{ lpm}$, $n = 500 \text{ rpm}$

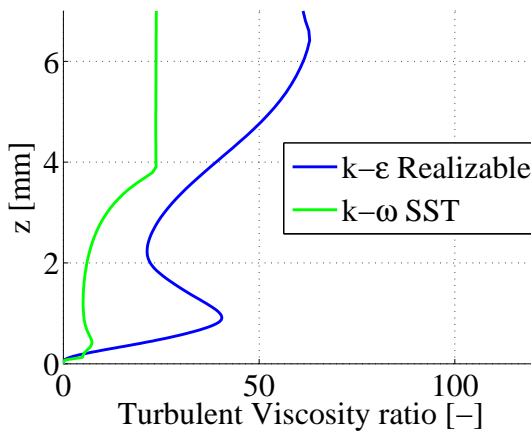


Figure 53: Turbulent viscosity ratio along the centerline with two different turbulence models, $h_{nd} = 35 \text{ mm}$, $Q = 1.5 \text{ lpm}$, $n = 500 \text{ rpm}$

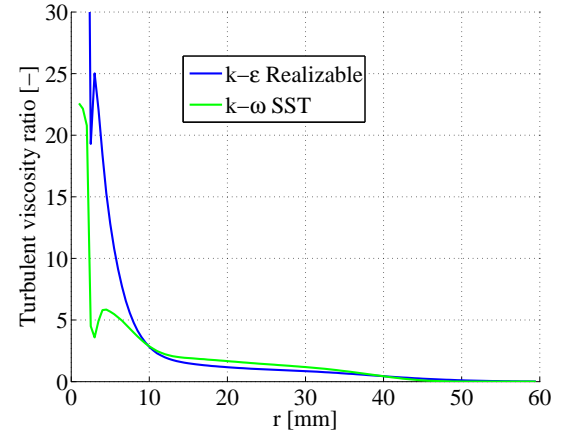


Figure 54: Time averaged mean turbulent viscosity ratio $\beta = \bar{v}_t/\nu_l$ with two different turbulence models, $h_{nd} = 35 \text{ mm}$, $n = 500 \text{ rpm}$, $Q = 1.5 \text{ lpm}$

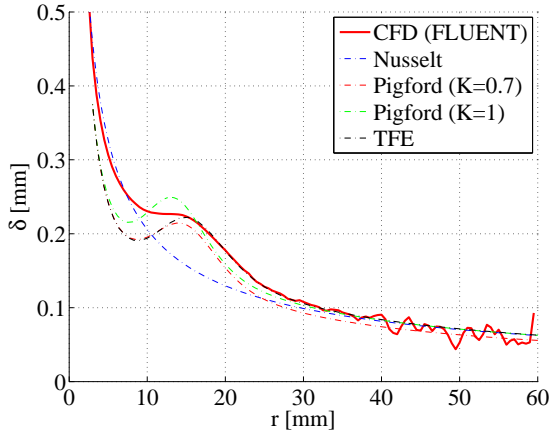


Figure 55: Time averaged film thickness, $n = 500 \text{ rpm}$, $Q = 0.3 \text{ lpm}$, $h_{nd} = 17.5 \text{ mm}$

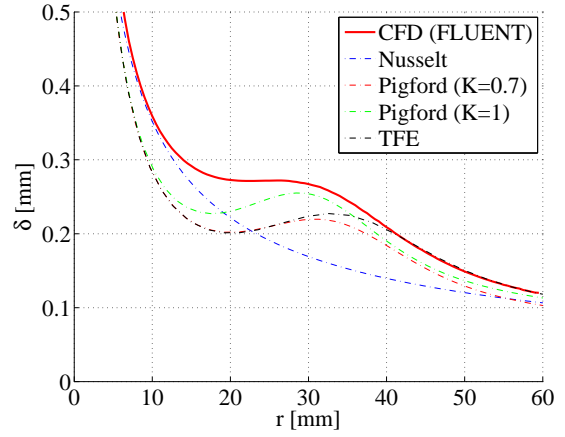


Figure 58: Time averaged film thickness, $n = 500 \text{ rpm}$, $Q = 1.5 \text{ lpm}$, $h_{nd} = 17.5 \text{ mm}$

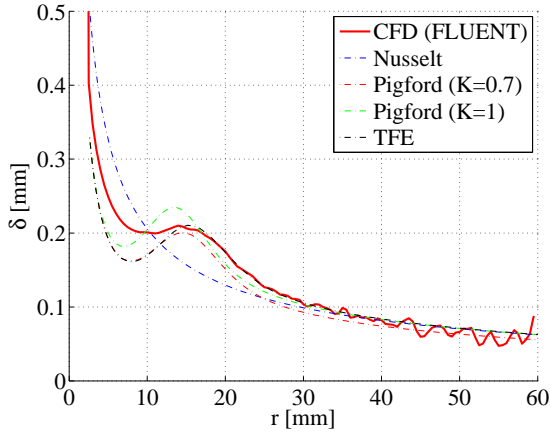


Figure 56: Time averaged film thickness, $n = 500 \text{ rpm}$, $Q = 0.3 \text{ lpm}$, $h_{nd} = 35 \text{ mm}$

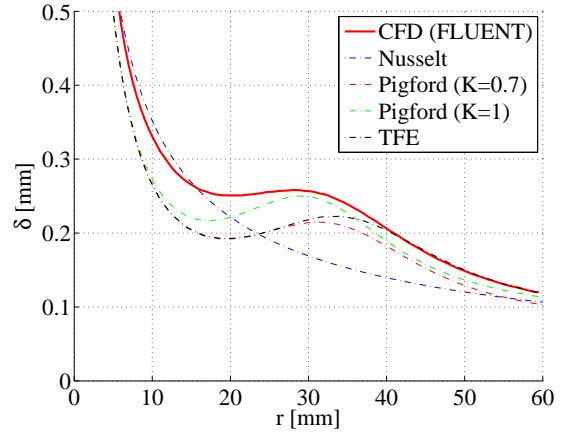


Figure 59: Time averaged film thickness, $n = 500 \text{ rpm}$, $Q = 1.5 \text{ lpm}$, $h_{nd} = 35 \text{ mm}$

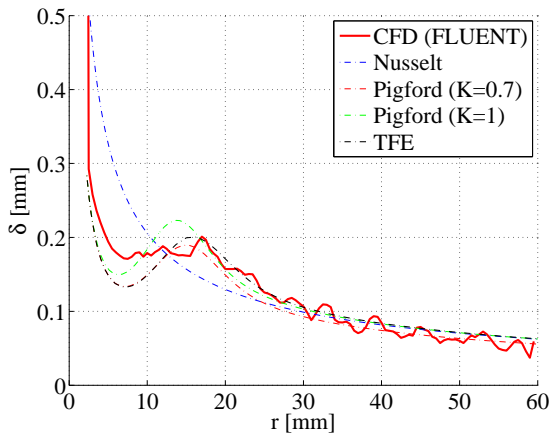


Figure 57: Time averaged film thickness, $n = 500 \text{ rpm}$, $Q = 0.3 \text{ lpm}$, $h_{nd} = 70 \text{ mm}$

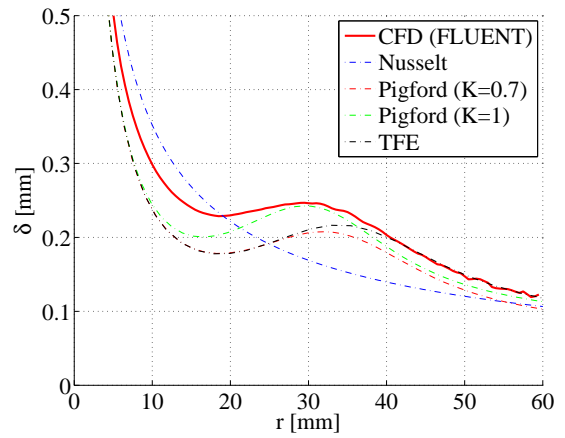


Figure 60: Time averaged film thickness, $n = 500 \text{ rpm}$, $Q = 1.5 \text{ lpm}$, $h_{nd} = 70 \text{ mm}$

The present TFE results have been obtained following the concept of Kim & Kim (2009), who assumed a quadratic (Eq. (116)) and a quartic polynomial (Eq. (122)) for the radial velocity to compute the convective non-linear terms and the wall gradients appearing in the depth-averaged TFE formulation, respectively. The validity of these profile assumptions shall be assessed by a comparison against the CFD results. The polynomials are assessed in a dimensional representation written as

$$u_{quadratic} = \frac{3}{2}\bar{u} (2\zeta - \zeta^2), \quad (166)$$

and

$$u_{quartic} = u_s \left(\frac{8}{5}\zeta - \frac{4}{5}\zeta^3 + \frac{1}{5}\zeta^4 \right) + \frac{r\delta^2}{5}\zeta (1 - \zeta)^2 \left(1 - \frac{\zeta}{2} \right) \left(\frac{\Omega^2}{\nu} \right) \quad (167)$$

with the velocity at the surface given by

$$u_s = \frac{25}{16}\bar{u} - \frac{r\delta^2}{48} \left(\frac{\Omega^2}{\nu} \right). \quad (168)$$

The wall-normal coordinate remains normalized with local film thickness

$$\zeta = \frac{z}{\delta}. \quad (169)$$

Figures 61 and 62 shows velocity profiles obtained from TFE for the laminar case 2b and the turbulent case 4b, respectively, plotted at selected radial positions compared against the corresponding CFD results. The different heights of the end points are due to the differently predicted film heights. The TFE solutions show in general no significant influence of the assumed polynomials. Compared against the CFD results a good agreement is seen for the laminar case for the larger radii. For the turbulent case shown in Figure 62 the TFE predictions agree very well only at the largest radius $r = 50 \text{ mm}$. In the inner radial region near the impingement the characteristic bulky turbulent profiles can evidently not be reproduced by neither of the assumed polynomials. The observed predictive limitations translate into the

predictions for the wall shear stress along the disk as seen from Figures 63-68.

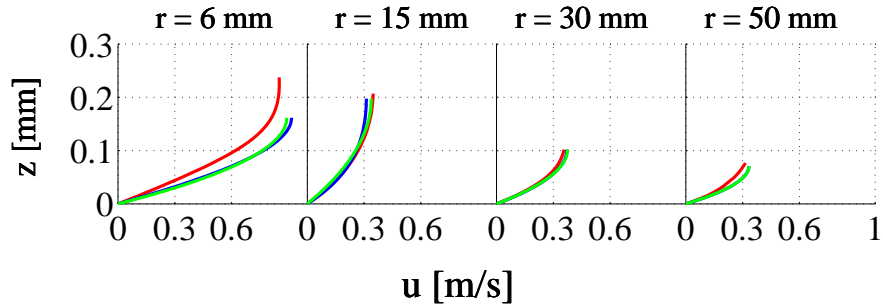


Figure 61: Radial velocity profiles at different radial positions, $n = 500 \text{ rpm}$, $Q = 0.3 \text{ lpm}$, $h_{nd} = 35 \text{ mm}$

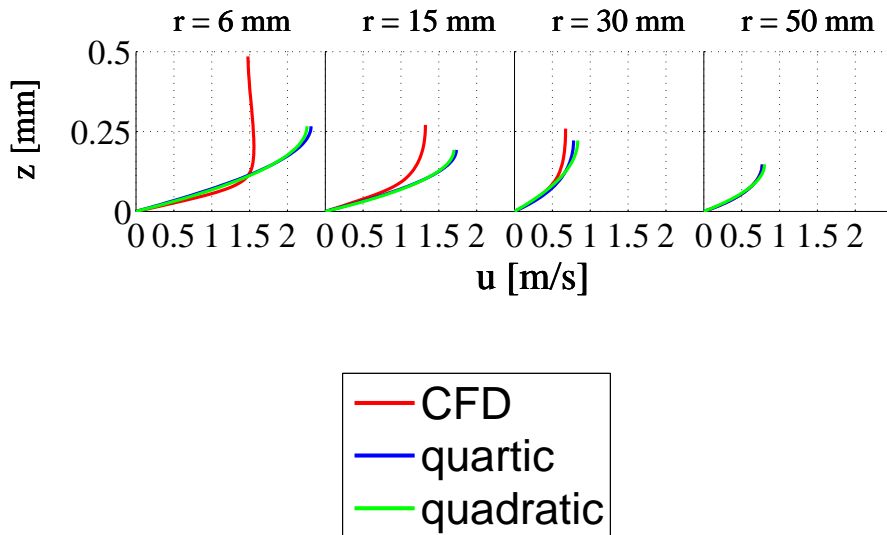


Figure 62: Radial velocity at profiles different radial positions, $n = 500 \text{ rpm}$, $Q = 1.5 \text{ lpm}$, $h_{nd} = 35 \text{ mm}$

Taking the derivative of the polynomials given by Eqs. (166) and (167) at the wall yields the TFE predictions

$$\tau_{w_{quadratic}} = \mu \frac{3\bar{u}}{\delta}, \quad (170)$$

and

$$\tau_{w_{quartic}} = \mu \frac{15\bar{u} + r\delta^2 \left(\frac{\Omega^2}{\nu}\right)}{6\delta}. \quad (171)$$

The comparison against the CFD solutions makes evident that characteristic peak next to the center, which is due to the formulation of a very thin velocity boundary layer starting from the stagnation point at $r = 0$, is completely missed by the TFE approach. This explains the generally underpredicted film heights near the center as observed in Figures 58-60. Radially further downstream the deviations become significantly smaller when approaching the outer disk radius. For the two higher rotational speeds the agreement is better in the laminar case, as seen from Figures 64 and 65 compared against Figures 66 and 67, respectively. For the lowest rotational speed the opposite is observed. It has still to be recognized that, the assumption of the quartic polynomial always leads to a better agreement with the CFD data.

The discrepancies observed for the profiles in Figures 61 and 62 have partly to be attributed to the considerable differences in the prediction of the local film thickness, as indicated by the different heights of the end points of the profiles. A more rigorous analysis of the descriptive capability of the assumed polynomials can eliminate this effect by comparing the profiles in a non-dimensional representation using for all the same reference quantities, δ and \bar{u} , taken from the CFD solutions at the considered radius. Figures 69 and 70 show such a comparison at two radial positions, where the CFD solution as well as the polynomials given by Eqs. (166) and (167) are non-dimensionalized with the same reference values \bar{u} and δ , which are predicted by the CFD simulation at the radii $r = 6 \text{ mm}$ and $r = 50 \text{ mm}$, respectively. In the laminar case ($Q = 0.3 \text{ lpm}$) good agreement between the CFD simulation

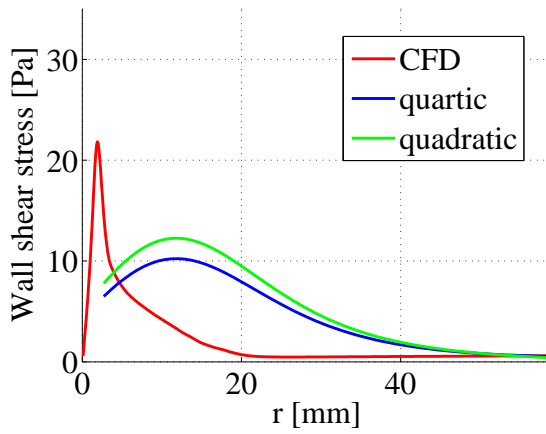


Figure 63: Time averaged wall shear stress, $n = 60 \text{ rpm}$, $Q = 0.3 \text{ lpm}$, $h_{nd} = 35 \text{ mm}$

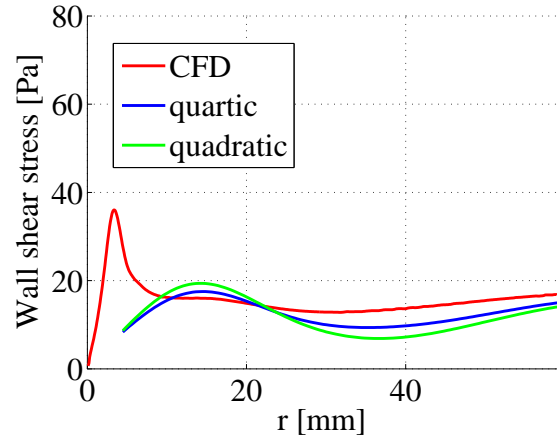


Figure 66: Time averaged wall shear stress, $n = 500 \text{ rpm}$, $Q = 1.5 \text{ lpm}$, $h_{nd} = 35 \text{ mm}$

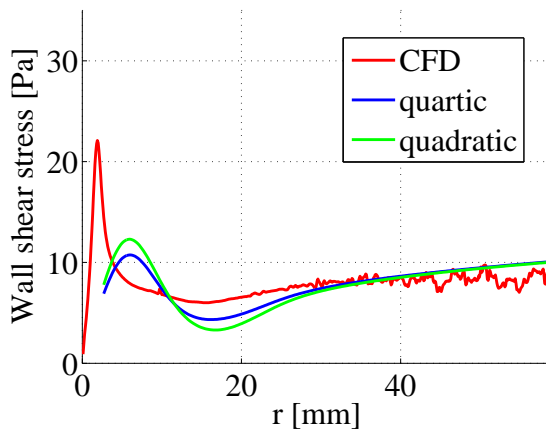


Figure 64: Time averaged wall shear stress, $n = 500 \text{ rpm}$, $Q = 0.3 \text{ lpm}$, $h_{nd} = 35 \text{ mm}$

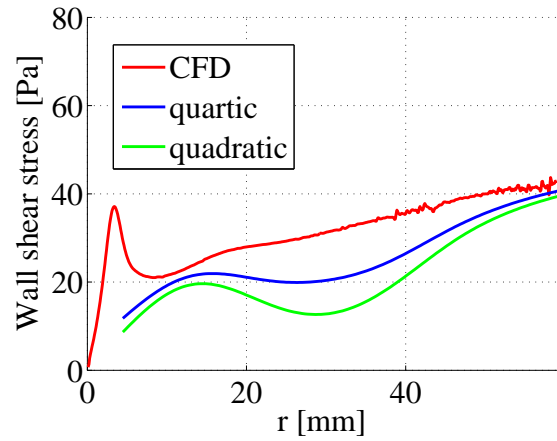


Figure 67: Time averaged wall shear stress, $n = 1000 \text{ rpm}$, $Q = 1.5 \text{ lpm}$, $h_{nd} = 35 \text{ mm}$

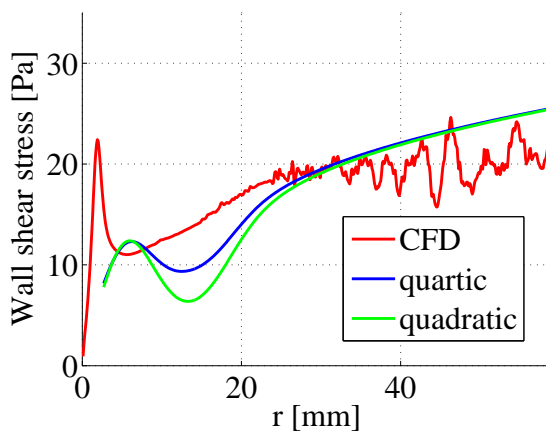


Figure 65: Time averaged wall shear stress, $n = 1000 \text{ rpm}$, $Q = 0.3 \text{ lpm}$, $h_{nd} = 35 \text{ mm}$

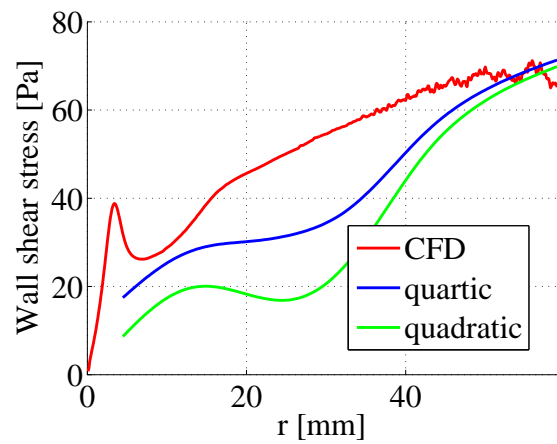


Figure 68: Time averaged wall shear stress, $n = 1500 \text{ rpm}$, $Q = 1.5 \text{ lpm}$, $h_{nd} = 35 \text{ mm}$

and the assumed velocity profiles is seen for both radial positions. In contrast, the bulky profile at the smaller radius in the turbulent case ($Q = 1.5 \text{ lpm}$) cannot be reflected by the polynomial profiles at all, and, hence, the gradients near the wall are much higher in the CFD results. At the larger radius the profiles are in a good agreement again. This has to be expected, because the flow is laminar in this outer radial region as seen from the vanishing turbulent viscosity ratio in Figure 41-43. It can be concluded that the shape of the assumed polynomials provide a very reliable description as long as the flow is laminar.

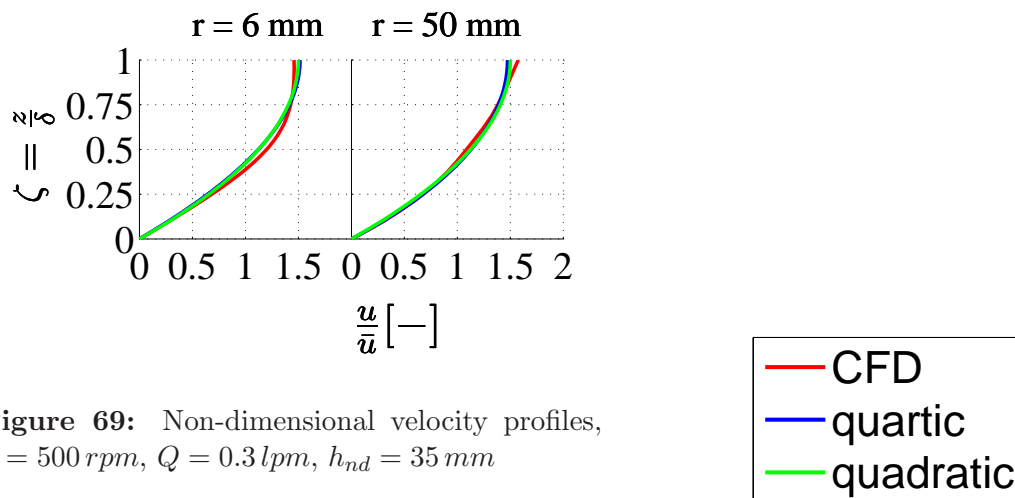


Figure 69: Non-dimensional velocity profiles, $n = 500 \text{ rpm}$, $Q = 0.3 \text{ lpm}$, $h_{nd} = 35 \text{ mm}$

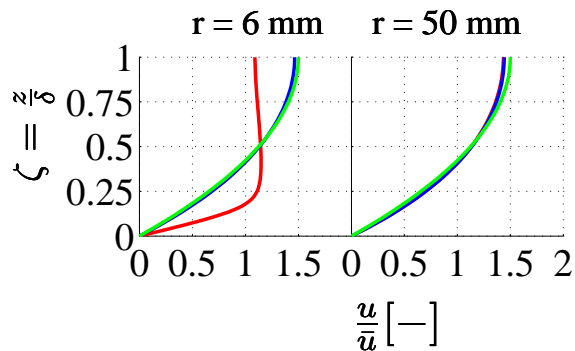


Figure 70: Non-dimensional velocity profiles, $n = 500 \text{ rpm}$, $Q = 1.5 \text{ lpm}$, $h_{nd} = 35 \text{ mm}$

5 Summary

- The influence of the nozzle-to-disk distance is basically restricted to the central region near the impingement point. The radial extension of this region of influence, r_{infl} , decreases with increasing rotational speed. A correlation, Eq. (158), is proposed, which was shown to provide a good estimate for r_{infl} .
- In the laminar cases associated with the lower considered flow rate the gravitational acceleration is relevant, and a higher nozzle-to-disk distance leads to a higher impingement velocity. This translates into higher initial radial velocities and, as a consequence, higher wall shear stresses near the impingement. Within $r < r_{infl}$, an enhanced etching activity can therefore be expected for a higher nozzle-to-disk distance in the case of laminar inflow, where the nozzle exit velocities are comparatively low.
- For the turbulent inflow conditions associated with the higher considered flow rate, the gravity-driven acceleration of the vertical jet does not significantly increase the momentum of the liquid at the impingement. Here, a shorter nozzle-to-disk distance was proven as favourable for the persistence of the turbulence level introduced at the nozzle, as well as favourable for the turbulence production radially next to the impingement point. The resulting higher level of turbulence observed for the smaller nozzle-to-disk distances lets expect a higher etching activity near the center for this case. In the outer radial region the turbulence level generally drops to zero, and the liquid flow becomes laminar. For high rotational speeds the wall shear stresses obtained in the radially outer region still exceed the peak values near the center, despite the turbulence-induced increase of the wall shear stress in the region around the impingement.
- In consistence with the general theory of liquid jet breakup, the laminar cases exhibit the formation of capillary waves, which increasingly

perturb the surface of the vertical liquid jet with increasing nozzle-to-disk distance. It is shown that all considered laminar cases associated with the lower volumetric flow rate lie well within the capillary breakup regime, where the presently observed capillary waves would finally lead to a breakup of the liquid into single droplets further downstream in the case of a free jet without impingement.

- A comparison of the simulation results from CFD with well established approximate solutions proposed for liquid film flow, the thin film equation (TFE) and Pigford model, show generally good agreement in the radially outer region for the film thickness, wall shear stress and velocity profiles. Significant deviations are generally observed in the central region, where the approximate solutions cannot predict the initial peak in the wall shear stress associated with formation of a very thin velocity boundary layer immediately downstream of the central impingement point. It is shown that the assumed quadratic and quartic polynomials for the radial velocity, as required by the TFE method, describe the shape of the profiles obtained from the CFD simulation very well, if the flow is laminar. The typically bulky turbulent profiles are missed completely instead.

List of symbols

Latin symbols:

a	model constant	-
a_1	model constant	-
A_0	model constant	-
A_S	model constant	-
b	model constant	-
C	model constant	-
$C_{1\epsilon}, C_2$	model constant	-
C_μ	model constant	-
CFL	Courant-Friedrich-Levy number	-
d_{nozzle}	diameter of the nozzle	m
d_{imp}	diameter of the jet at impact	m
D_ω^+	positive portion of the cross-diffusion term	N/m^4
F_1, F_2	blending function	-
g	gravitational acceleration	m/s^2
G_k	production of the turbulent kinetic energy	m^2/s^3
h_{nd}	nozzle-to-disk distance	m
h_{out}	radially outer height of computational domain	m
I	turbulent intensity	%
k	turbulent kinetic energy	m^2/s^2
k_s	roughness height	m
k_s^+	non-dimensionall roughness height	-
K	model parameter	-
l_0	length scale	m
n	rotational speed	rpm
\hat{n}_w	normal unit vector	-
Oh	Ohnesorge number	-
p	static pressure	Pa

Q	volumetric flow rate	m^3/s
r	radial position	m
r_{infl}	radial extension of region of influence h_{nd}	m
r_δ	radial position of interface	m
R_{max}	radial extension of the disk	m
R_i	radial extension of computational domain around the vertical jet	m
R_k	model constant	—
Re	Reynolds number	-
S	modulus of the mean rate-of-strain	$1/s$
S_{ij}	strain tensor	$1/s$
t	time	s
\hat{t}_w	tangential unit vector	—
u	radial velocity	m/s
u^+	non-dimensional velocity	—
\bar{u}	radial mean velocity of the liquid film	m/s
u_τ	wall friction velocity	m/s
$u_{quadratic}$	quadratic polynomial velocity profile	m/s
$u_{quartic}$	quartic polynomial velocity profile	m/s
\bar{v}	tangential mean velocity of the liquid film	m/s
v_B	velocity obtained from Bernoulli equation	m/s
v_c	centerline velocity	m/s
v_{imp}	velocity of the jet at impact	m/s
v_{nozzle}	nozzle exit velocity	m/s
W	Weber number	-
y^+	non-dimensional distance from wall	-
Y_k	dissipation of the turbulent kinetic energy	m^2/s^3
Y_ω	destruction of the specific dissipation	N/m^2s
z	vertical coordinate	m

Greek symbols:

$\bar{\alpha}$	normalized volume fraction	-
α_f	face volume fraction	-
α_f^*	modified face volume fraction	-
α_A	volume fraction of the acceptor cell	-
α_D	volume fraction of the donor cell	-
α_U	volume fraction of the upwind cell	-
$\alpha, \alpha^*, \alpha_\infty, \alpha_\infty^*$	model constants	-
α_q	volume fraction of phase q	-
β	turbulent viscosity ratio	-
β_i	model constant	-
β_∞^*	model constant	-
β_{i1}, β_{i2}	model constant	-
Γ	blending function	-
Γ_k	effective diffusivities for turbulent kinetic energy	m^2/s
Γ_ω	effective diffusivities for specific dissipation	m^2/s
δ	liquid film thickness	m
δ_0	length scale	m
ϵ	turbulent dissipation rate	m^2/s^3
ζ	axial distance from the nozzle	m
Θ_w	contact angle	
μ_t	turbulent dynamic viscosity of the liquid film	Ns/m^2
ν_g	molecular kinematic viscosity of gaseous phase	m^2/s
ν_l	molecular kinematic viscosity of liquid phase	m^2/s
ν_t	turbulent viscosity of the liquid film	m^2/s

ν_{tot}	total viscosity	m^2/s
ρ	density of the fluid	kg/m^3
ρ_g	density of gaseous phase	kg/m^3
ρ_l	density of liquid phase	kg/m^3
σ	surface tension	kg/s^2
$\sigma_k, \sigma_\epsilon, \sigma_\omega$	model constant	—
σ_{k1}, σ_{k2}	model constant	—
$\sigma_{\omega1}, \sigma_{\omega2}$	model constant	—
τ_w	wall shear stress	$kg/(ms^2)$
Φ_1, Φ_2	blending function	-
ω	specific turbulent dissipation	$1/s$
Ω	angular velocity	rad/s

Sub- and superscripts:

$()^*$	non-dimensional quantity
$()_0$	reference value

References

- BRACKBILL, J. U., KOTHE, D. B. & ZEMACH, C. 1992 A continuum method for modeling surface tension. *Journal of Computational Physics* **100**, 335–354.
- CHARWAT, A. F., KELLY, R. E. & GAZLEY, C. 1972 The flow and stability of thin liquid films on a rotating disk. *Journal of Fluid Mechanics* **53** (02), 227.
- HIRT, C. W. & NICHOLS, B. D. 1981 Volume of fluid (vof) method for the dynamics of free boundaries. *Journal of Computational Physics* **39**, 201–225.
- KADER, B. 1981 Temperature and concentration profiles in fully turbulent boundary layers. *Int. J. Heat Mass Transfer* **24**, 1541–1544.
- KIM, TAE-SUNG & KIM, MOON-UHN 2009 The flow and hydrodynamic stability of a liquid film on a rotating disc. *Fluid Dynamics Research* **41** (3), 035504.
- LANDRETH, C. C. & ADRIAN, R. J. 1990 Impingement of a low reynolds number turbulent circular jet onto a flat plate at normal incidence. *Experiments in Fluids* **9** (1), 74–84.
- LENEWEIT, GERO, ROESNER, KARL G. & KOEHLER, REINHARD 2003 Effect of surfactants on the stability of thin liquid film flow on a rotating disk. *Journal of colloid and interface science* **260** (2), 349–360.
- LESHEV, I. & PEEV, G. 2003 Film flow on a horizontal rotating disk. *Chemical Engineering and Processing: Process Intensification* **42** (11), 925–929.
- LIU, X., V, J. H. LIENHARD & LOMBARA, J. S. 1991 Convective heat transfer by impingement of circular liquid jets. *Journal of Heat Transfer* **113**, 571–583.
- MENTER, F. R. 1994 Two-equation eddy-viscosity turbulence models for engineering applications. *AIAA Journal* **32** (8), 1598–1605.

- MIYASAKA, Y. 1974a On the flow of a viscous free boundary jet on a rotating disk : 1st report theoretical analysis. *Bulletin of JSME* **17** (113), 1461–1468.
- MIYASAKA, Y. 1974b On the flow of a viscous free boundary jet on a rotating disk : 2nd report comparison of experimental results with calculated values by means of film thickness. *Bulletin of JSME* **17** (113), 1469–1475.
- MUZAFERIJA, S., PERIC, M., SAMES, P. & SCHELLIN, T. 1998 A two-fluid navier-stokes solver to simulate water entry. *In Proc 22nd Symposium on Naval Hydrodynamics* pp. 277–289.
- OHNESORGE, WOLFGANG V. 1936 Die bildung von tropfen an düsen und die auflösung flüssiger strahlen. *ZAMM - Journal of Applied Mathematics and Mechanics* **16** (6), 355–358.
- OZAR, B., CETEGEN, B. M. & FAGHRI, A. 2003 Experiments on the flow of a thin liquid film over a horizontal stationary and rotating disk surface. *Exp. Fluids* **34**, 556–565.
- RAUSCHER, J. W., KELLY, R. E. & COLE, J. D. 1973 An asymptotic solution for the laminar flow of a thin film on a rotating disk. *Journal of Applied Mechanics* **40** (1), 43–47.
- RICE, JEREMY, FAGHRI, AMIR & CETEGEN, BAKI 2005 Analysis of a free surface film from a controlled liquid impinging jet over a rotating disk including conjugate effects, with and without evaporation. *International Journal of Heat and Mass Transfer* **48** (2526), 5192–5204.
- SHIH, TSAN-HSING, LIOU, WILLIAM W., SHABBIR, AAMIR, YANG, ZHI-GANG & ZHU, JIANG 1995 A new k- ϵ eddy viscosity model for high reynolds number turbulent flows. *Computers and Fluids* **24** (3), 227–238.
- SISOEV, G. M., MATAR, O. K. & LAWRENCE, C. J. 2003 Axisymmetric wave regimes in viscous liquid film flow over a spinning disk. *Journal of Fluid Mechanics* **495**, 385–411.

- STEVENS, J. & WEBB, B. W. 1993 Measurements of flow structure in the radial layer of impinging free-surface liquid jets. *International Journal of Heat and Mass Transfer* **36** (15), 3751–3758.
- TIVERT, T., BORGY, A., MARIMON, J. & DAVIDSON, L. 2007 Wind-driven rivulet over an edge with break-up. *6th International Conference on Multiphase Flow* pp. 1–9.
- WOOD, R. M. & WATTS, B. E. 1973 The flow, heat mass transfer characteristics of liquid film on rotating discs. *Transactions of the Institution of Chemical Engineers* (51), 315–322.